Examples for applications of scintillation counters measuring extensive air showers

http://particle.astro.ru.nl/goto.html?astroinst2021

KArlsruhe Shower Core and Array DEtector

Simultaneous measurement of
electromagnetic,
muonic,
hadronic
shower components

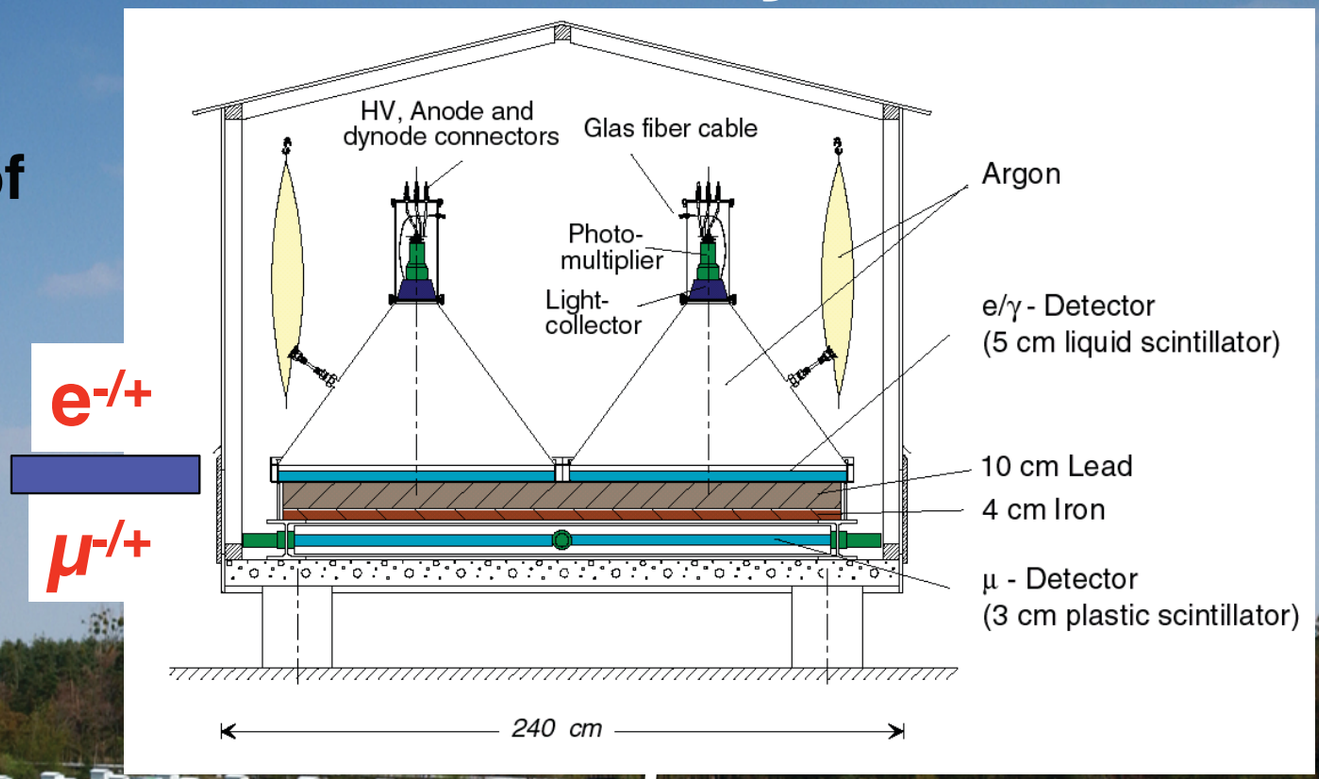

T. Antoni et al, Nucl. Instr. & Meth. A 513 (2004) 490

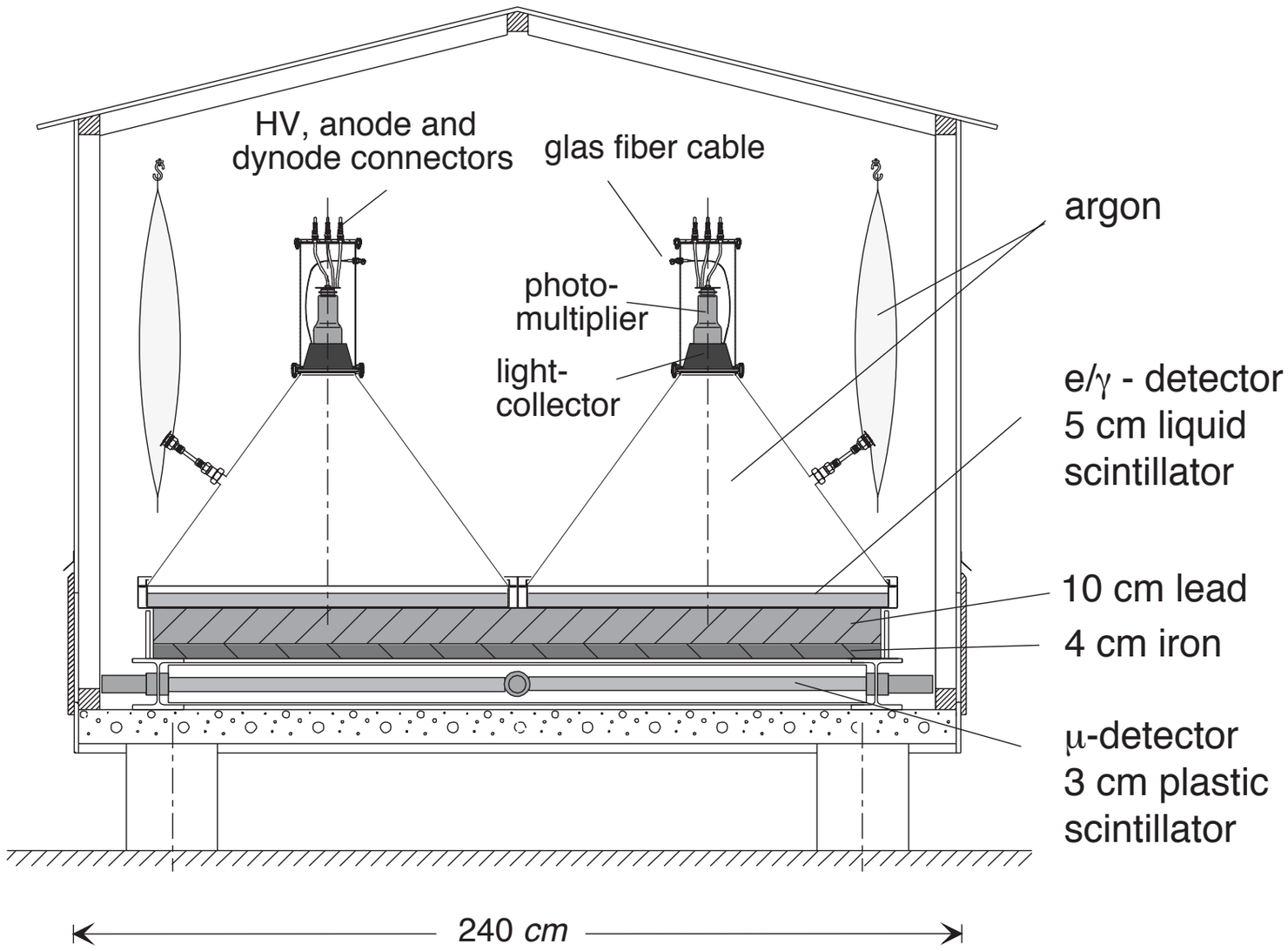

Fig. 4. Sketch of a fully equipped array station with four e/γ detectors on top of a Pb/Fe absorber plate and a segmented muon detector.

PDP liquid scintillator:
2 g/l PMP 1-phenyl-3-mesityl-2-pyrazoline
in 80% (volume) paraffin and 20% pseudocumbne

scintillating decay time: 2.5 ns
good transparency, working at low temperatures

PMTs: EMI 9822 and Valvo XP3462

8% energy resolution at 12 MeV
time resolution (passing muons): 0.77 ns

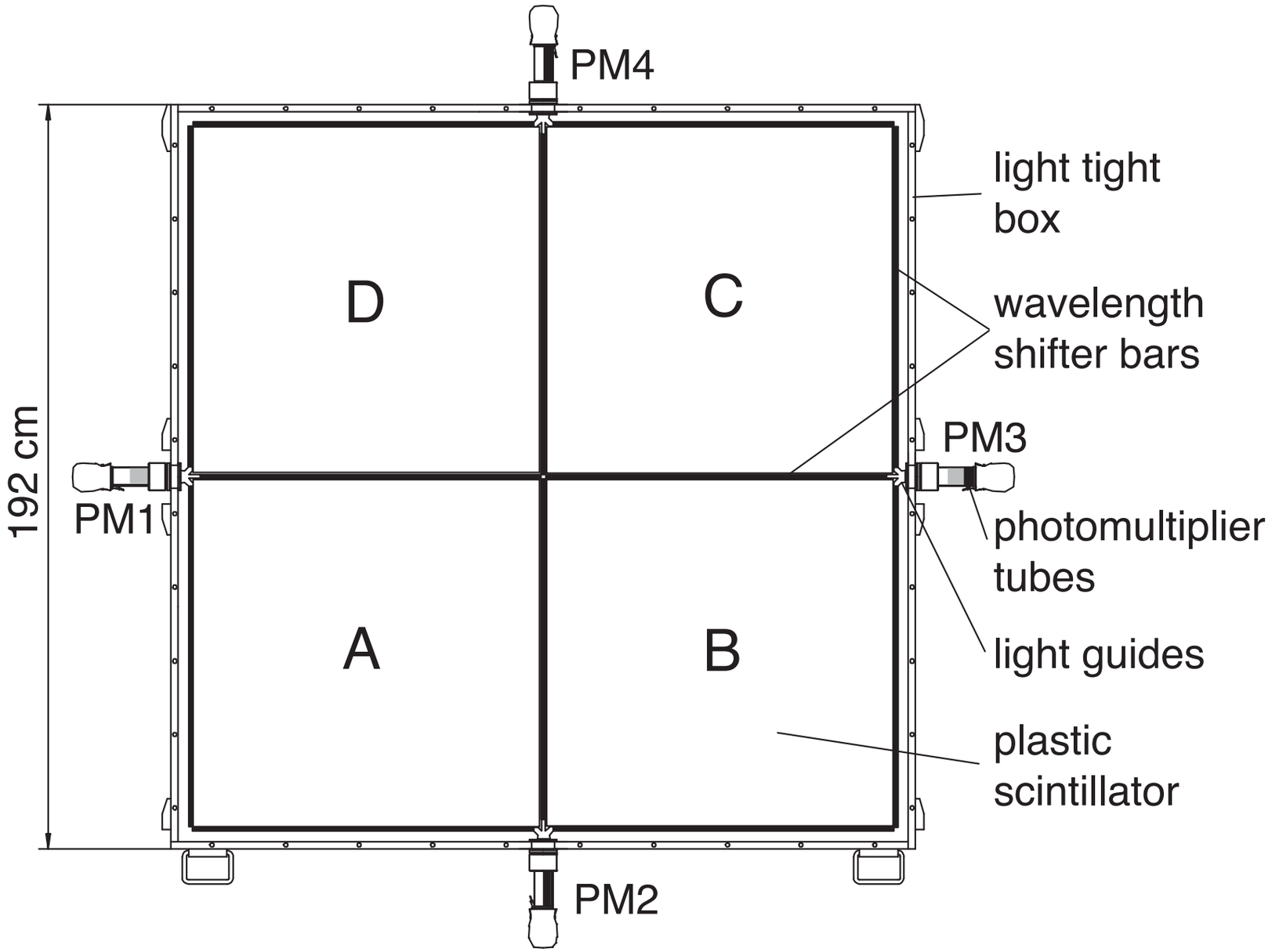

Fig. 6. Sketch of a muon detector in an array detector station.

four 3 cm thick plastic scintillators: Bicron BD-416 (90 cm x 90 cm)
PMTs 1,5“ EMI 9902 or Valvo XP2081

2% spacial non-uniformity
time resolution: 2.9 ns
energy resolution: 10% at 8 MeV

Event reconstruction in the scintillator array

electromagnetic component

shower core	$\Delta r = 2.5 - 5.5$ m
shower direction	$\Delta\theta = 0.5° - 1.2°$
shower size	$\Delta N_e/N_e = 6 - 12$ %

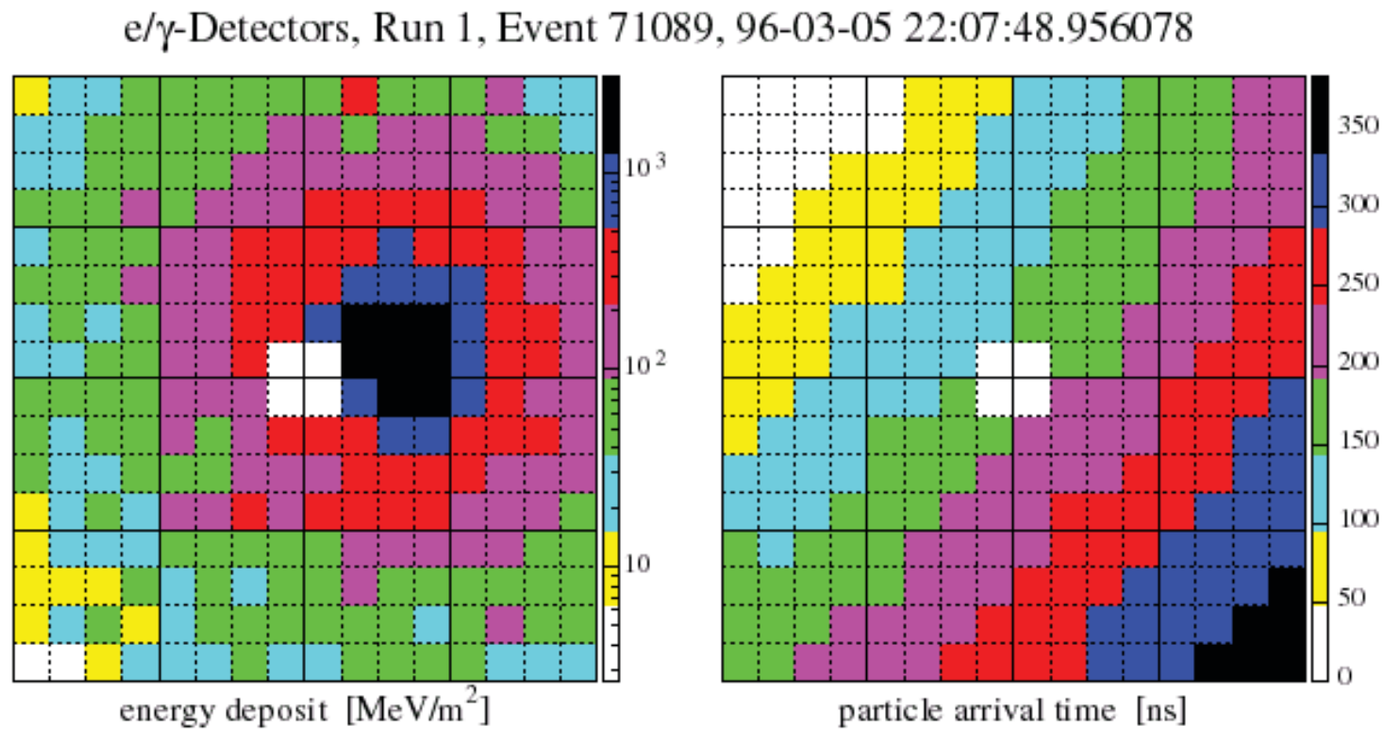

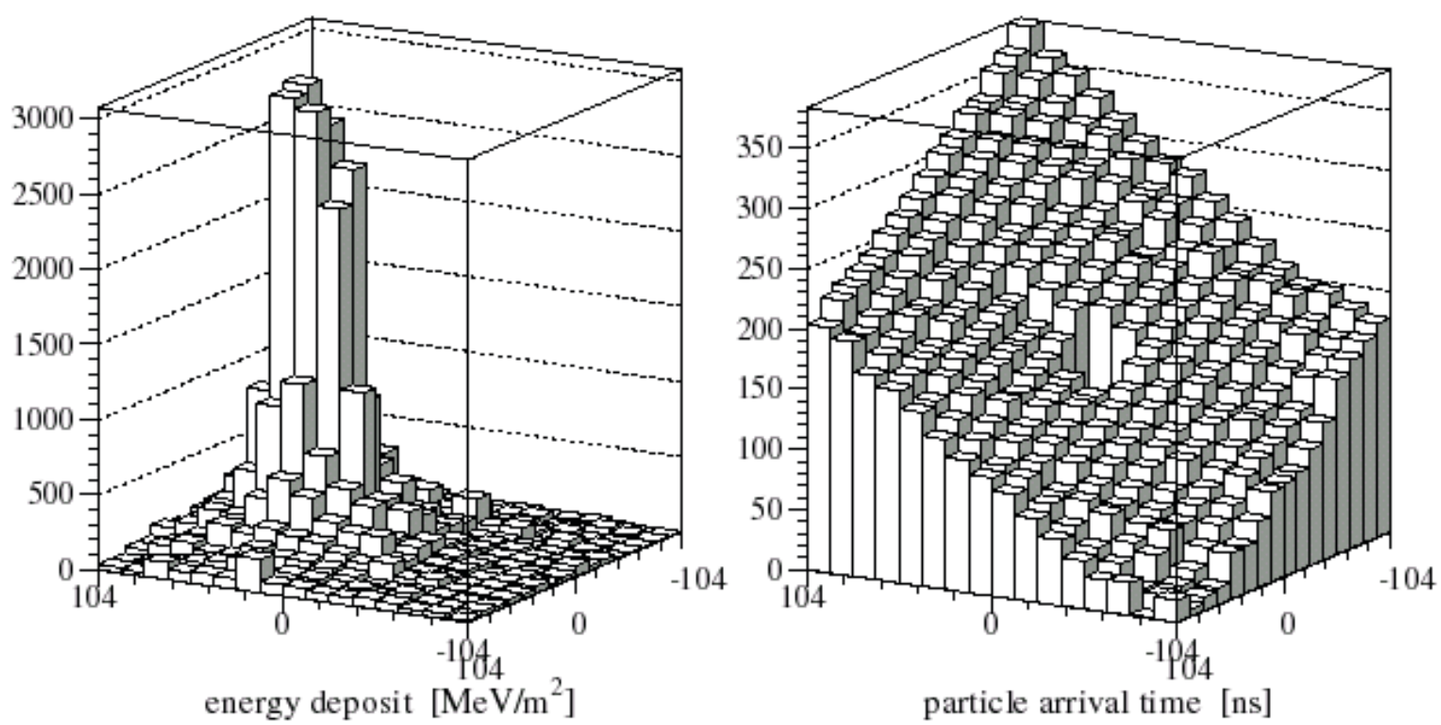

KASCADE GRANDE Array

37 detector stations

370 m² e/γ: scintillation counter

KASCADE

200 m x 200 m

700 m

700 m

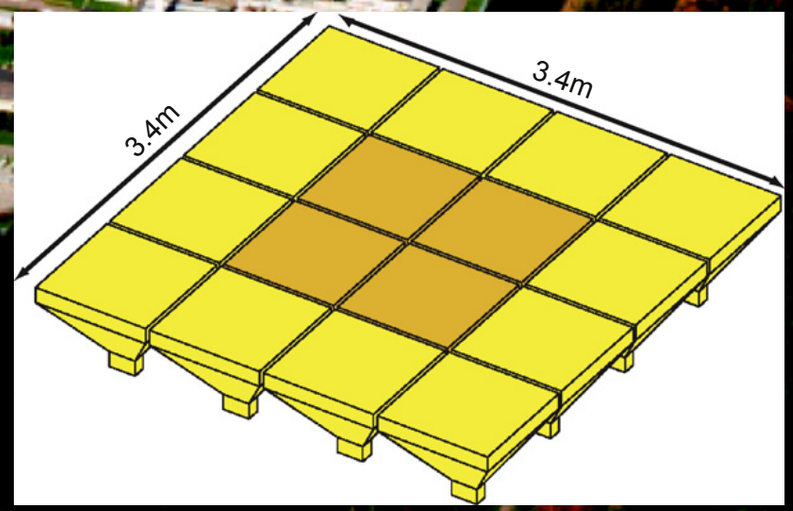

G. Navarra et al., Nucl Instr & Meth A 518 (2004) 207

Nuclear Instruments and Methods in Physics Research A 620 (2010) 202–216

Contents lists available at ScienceDirect

Nuclear Instruments and Methods in Physics Research A

journal homepage: www.elsevier.com/locate/nima

The KASCADE-Grande experiment

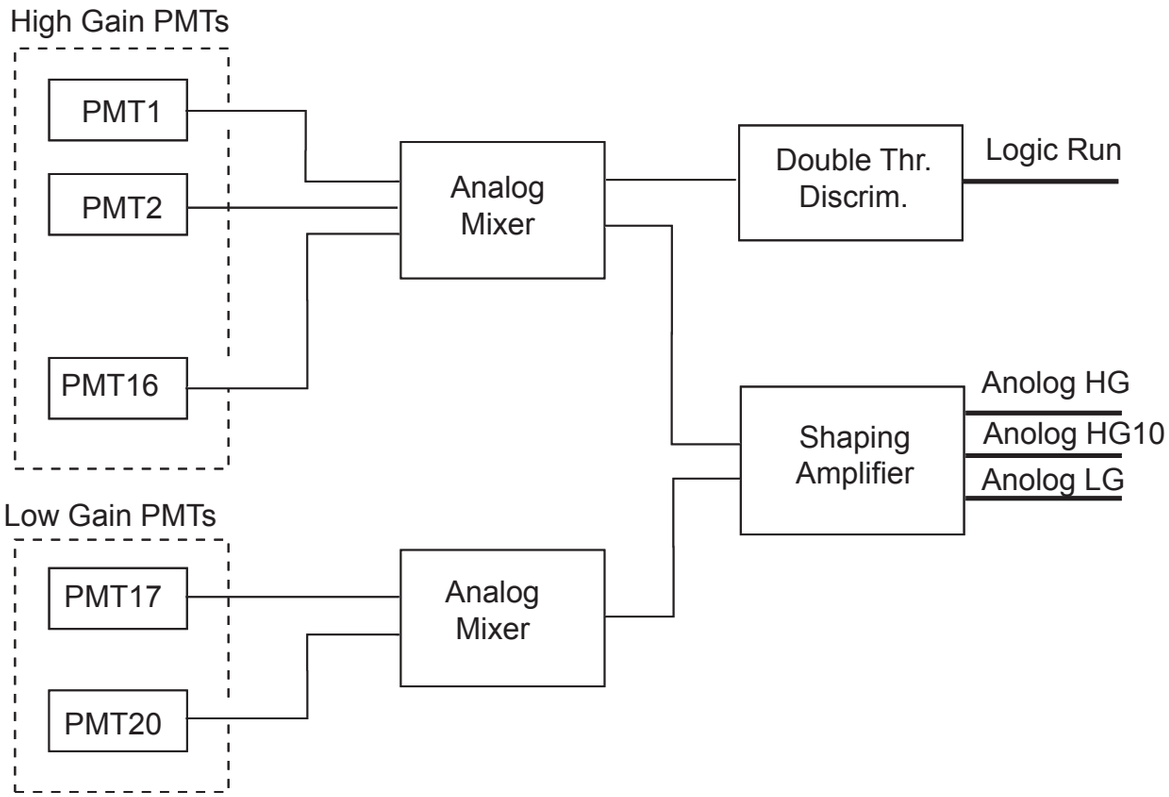

Fig. 6. Scheme of the electronics of an individual Grande detector station (only measurement channels are shown).

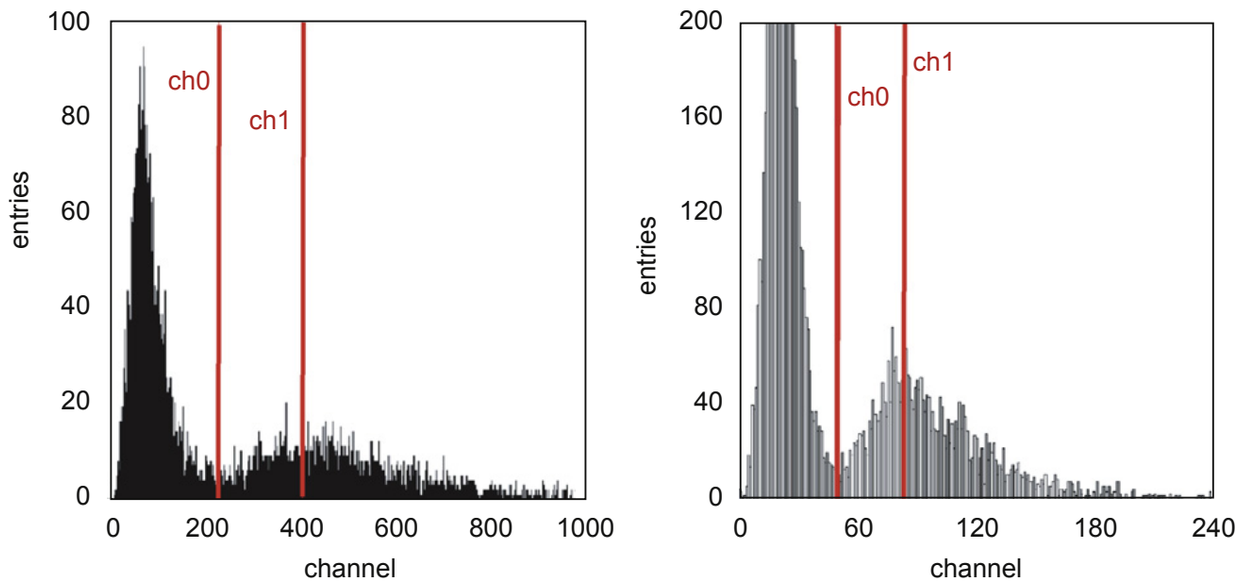

Fig. 8. Example of single particle spectra of HG (left panel) and LG (right panel) channels, used for gain equalization through the high voltage setting.

Bethe Bloch gives mean energy loss
thin absorbers: large fluctuations
energy loss can be described by a Landau function

$$\mathcal{L}(x) = \frac{1}{\sqrt{2\Gamma}} \exp\left(-\frac{1}{2}(\lambda + e^{-\lambda})\right)$$

$$\lambda = \frac{\Delta E - \Delta E^{mp}}{\xi}$$

ΔE **true energy loss in layer**

ΔE^{mp} **most probable energy loss in layer**

$$\xi = \kappa \cdot \rho \cdot x$$

x **thickness of absorber [cm]**

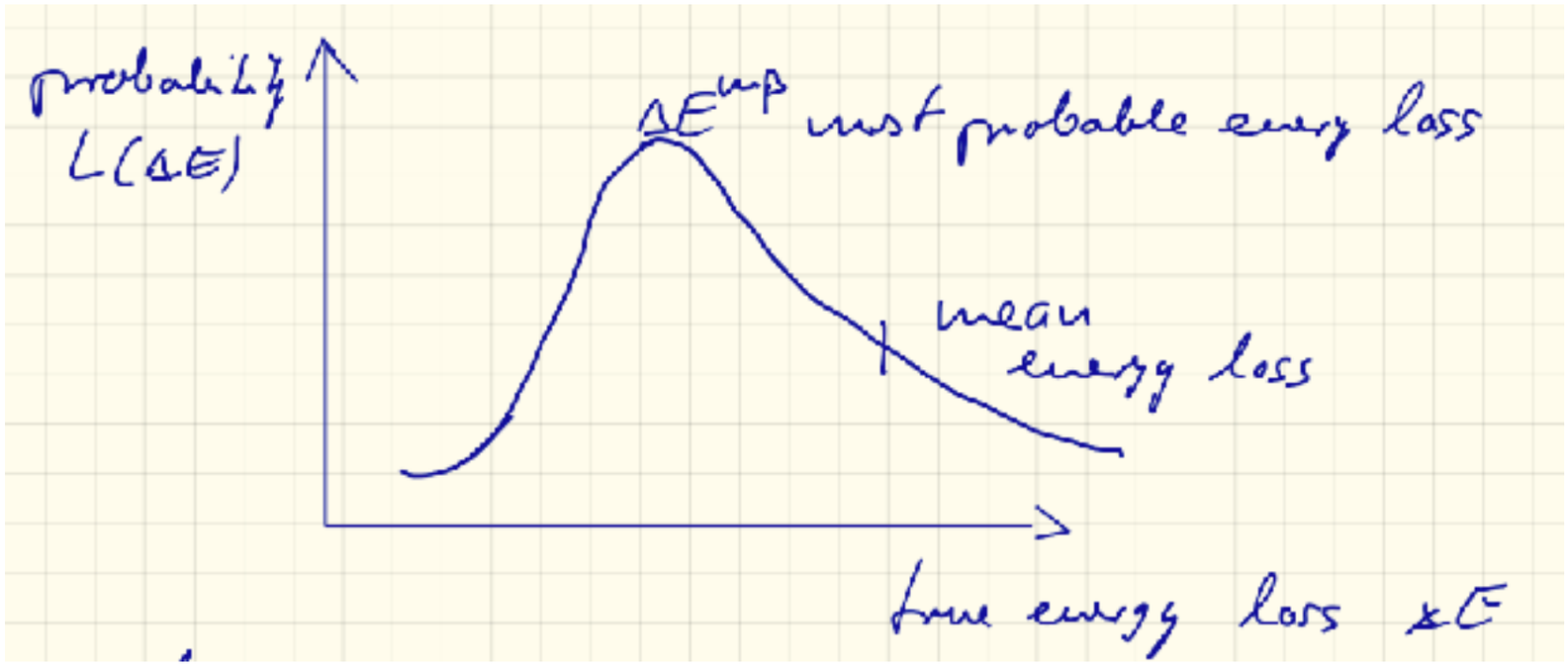

for electrons in Argon

$$\Delta E^{mp} = \xi \left\{ \ln \left[\frac{2 m_e c^2 \gamma^2 \beta^2}{I^2} \xi \right] - \beta^2 + 0.423 \right\}$$

energy loss of MIP $\beta\gamma \approx 4$

1 cm argon ΔE^{mp} **= 1.2 keV** $\Delta E_{BB} = 2.69$ **keV**

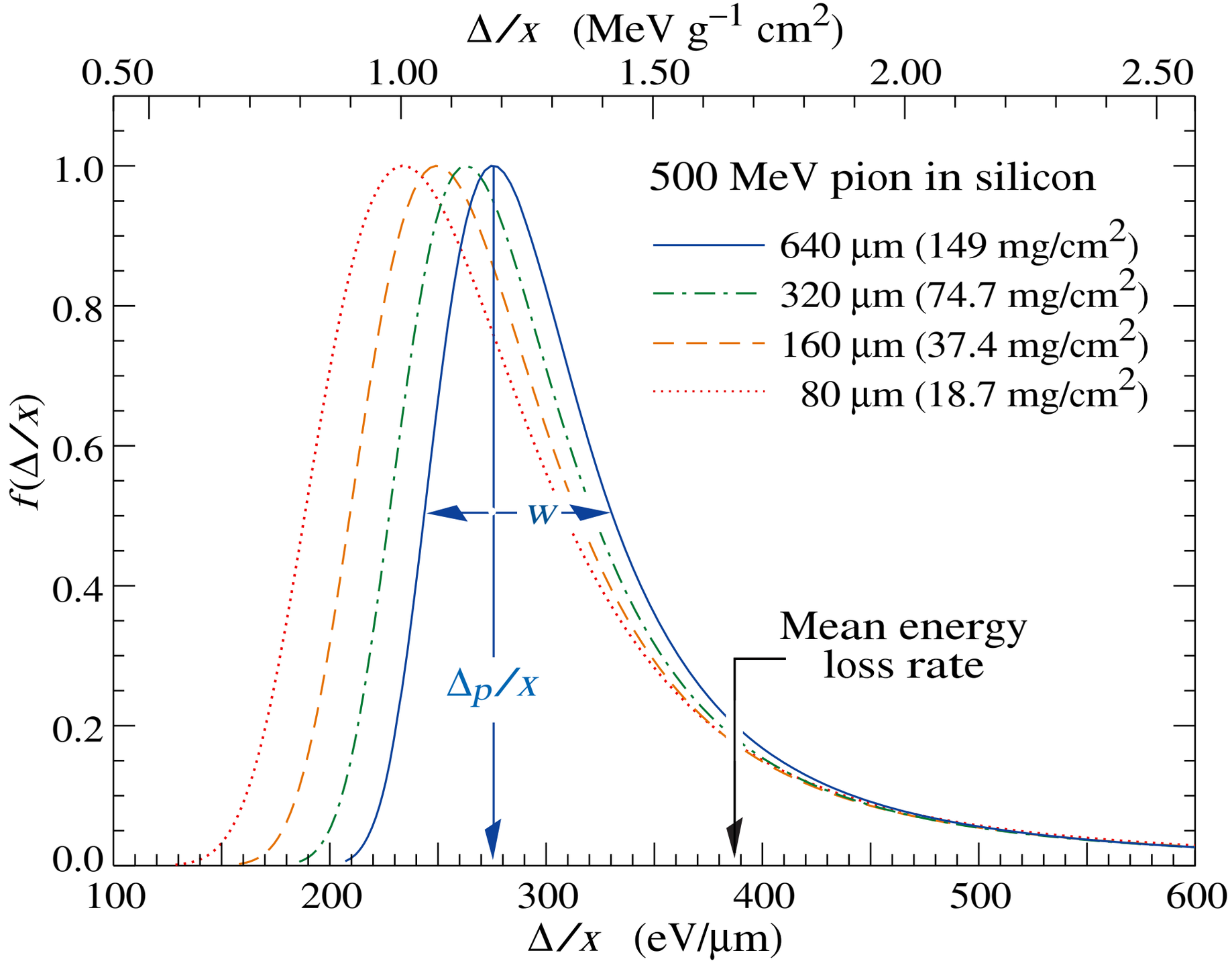

Figure 27.7: Straggling functions in silicon for 500 MeV pions, normalized to unity at the most probable value δ_p/x. The width w is the full width at half maximum.

Nuclear Instruments and Methods in Physics Research A 767 (2014) 339–346

Contents lists available at ScienceDirect

Nuclear Instruments and Methods in Physics Research A

journal homepage: www.elsevier.com/locate/nima

LORA: A scintillator array for LOFAR to measure extensive air showers

S. Thoudam [a,*], S. Buitink [a,b], A. Corstanje [a], J.E. Enriquez [a], H. Falcke [a,c,d], W. Frieswijk [c], J.R. Hörandel [a,d], A. Horneffer [a,1], M. Krause [a,2], A. Nelles [a,d], P. Schellart [a], O. Scholten [b], S. ter Veen [a], M. van den Akker [a]

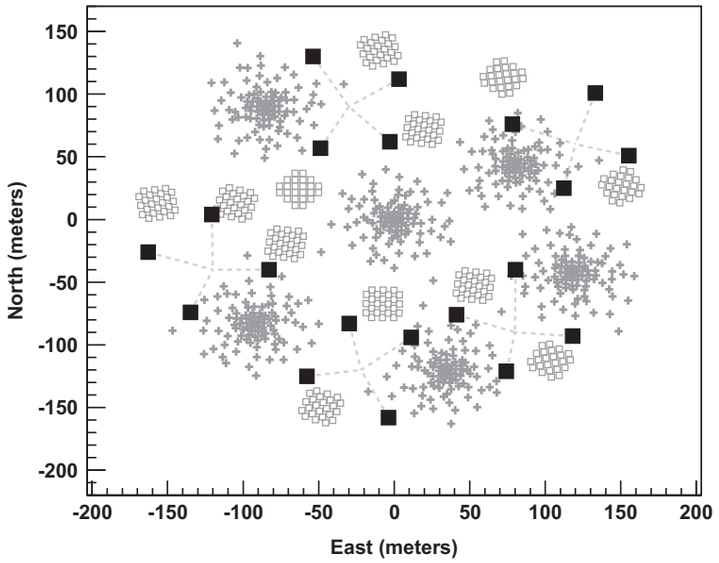

Fig. 1. Layout of LORA in the dense core in the center of LOFAR. The squares represent the positions of the particle detectors. The crosses and open squares represent the two different types of LOFAR radio antennas. The dotted lines indicate the grouping of the detectors for the data acquisition.

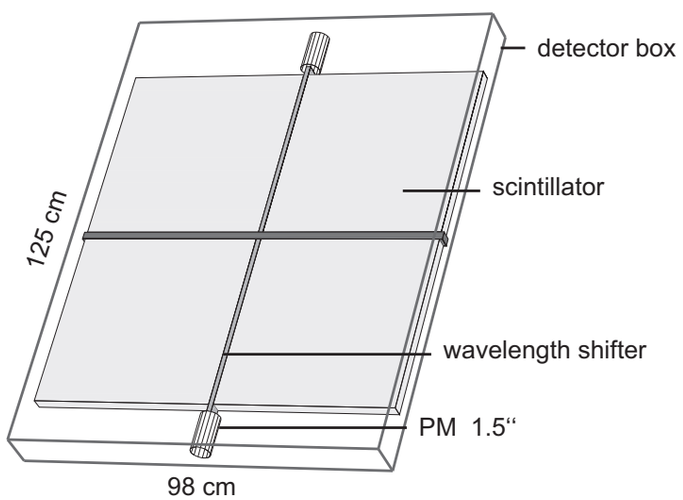

Fig. 2. Schematic view of a scintillation detector. Sheets of plastic scintillator are read out by photomultiplier tubes via wavelength shifter bars [14].

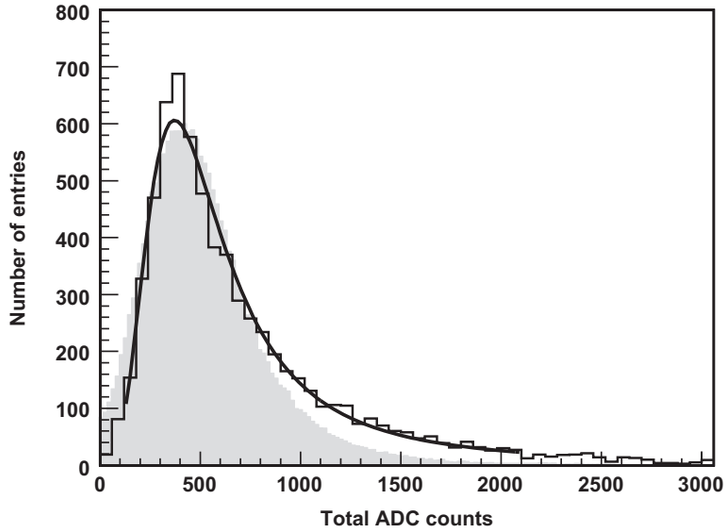

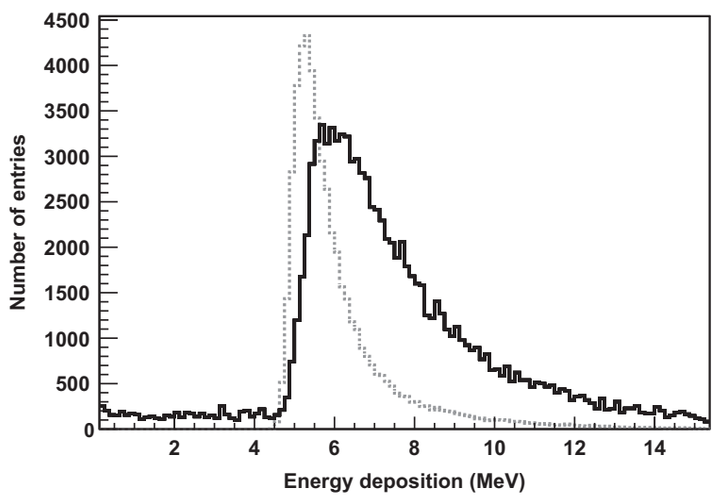

Fig. 5. Distribution of the total energy deposition by singly charged particles in detector. Top: measured values, the curve represents a fit of a Landau distributio function. The most probable value, given by the fit is (400.5 ± 3.5) ADC counts. Th predictions of a detector simulation using GEANT4 are indicated by the shade histogram. Bottom: results of a simulation, using the GEANT4 code for vertica muons (dotted histogram) and muons, impinging according to a $\cos(\theta)^2$ zenit angle distribution (solid histogram). The most probable energy deposition amount to 6.67 MeV.

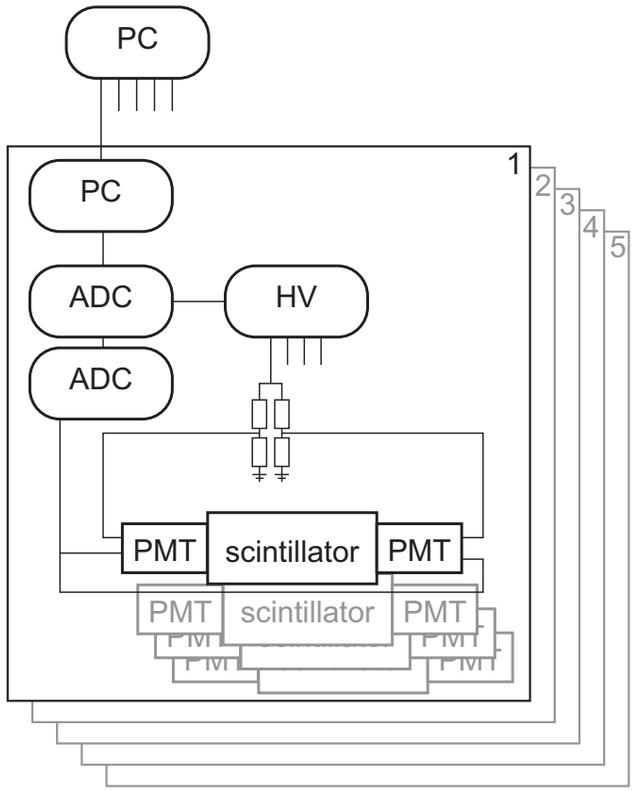

Fig. 3. Schematic view of the electronics components for the data acquisition and experiment control. A basic electronics unit serves to read out four scintillator units. Five such electronics units are used to read out the 20 detectors.

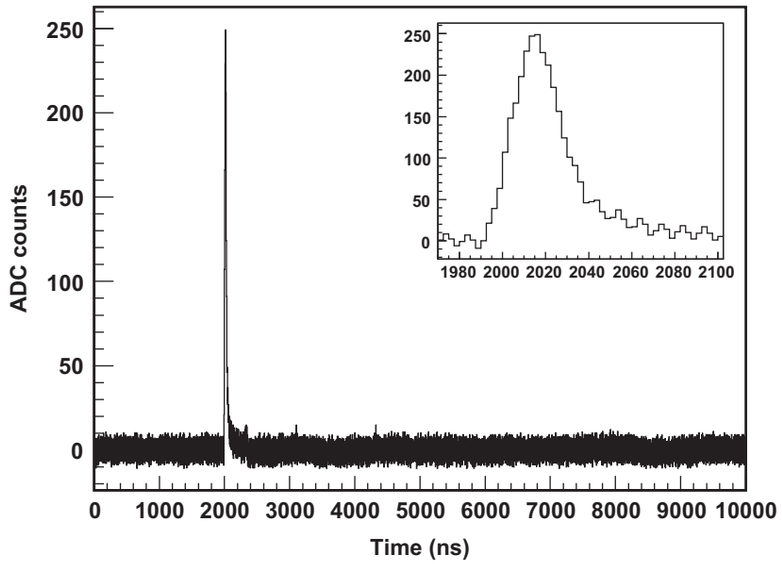

Fig. 4. Example of a signal time trace, produced by a charged particle pas though a detector. The inset shows a closer view of the signal around the maxin value (between 1970 and 2100 ns).

LOFAR Radboud Air Shower Array - LORA

20 scintillator units (~1 m² each) in LOFAR core

provide

- properties of EAS
- and trigger

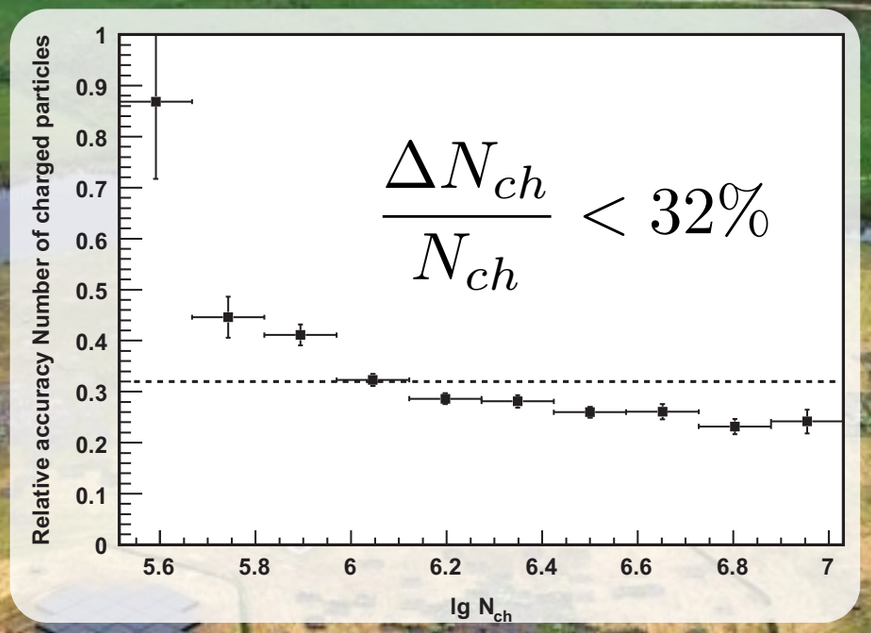

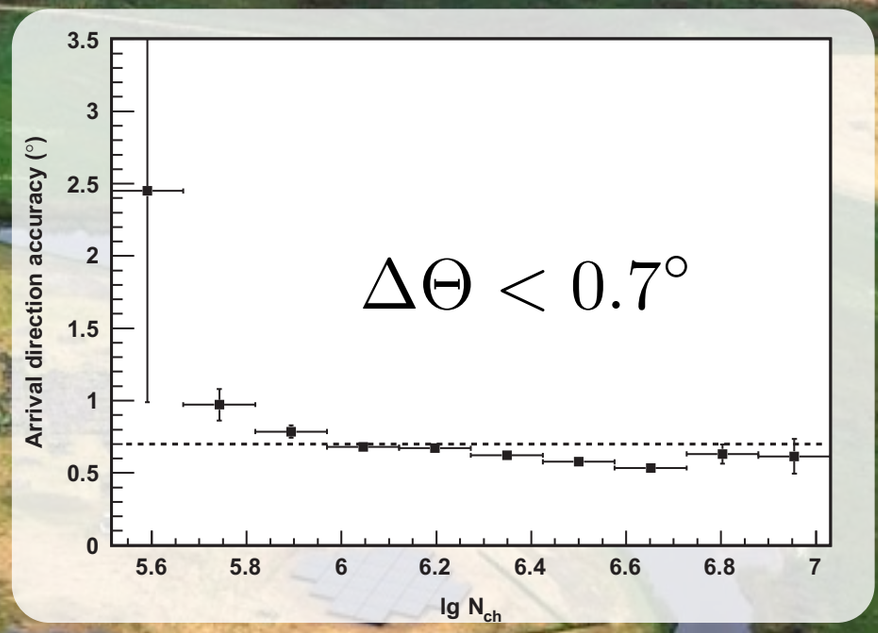

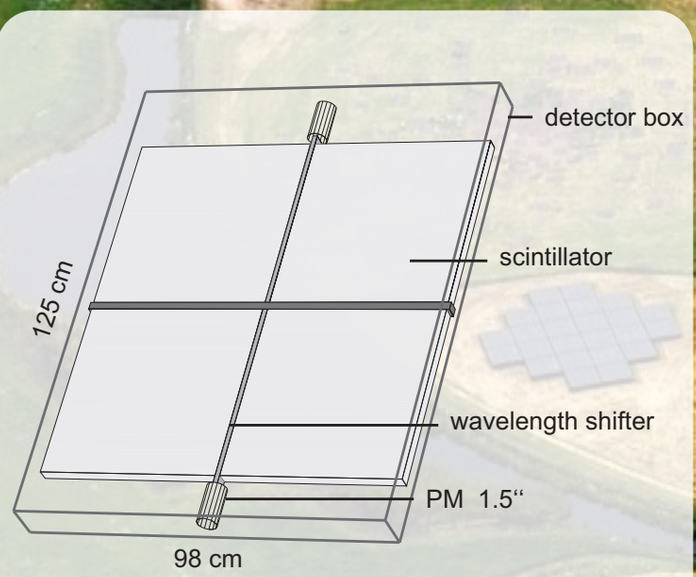

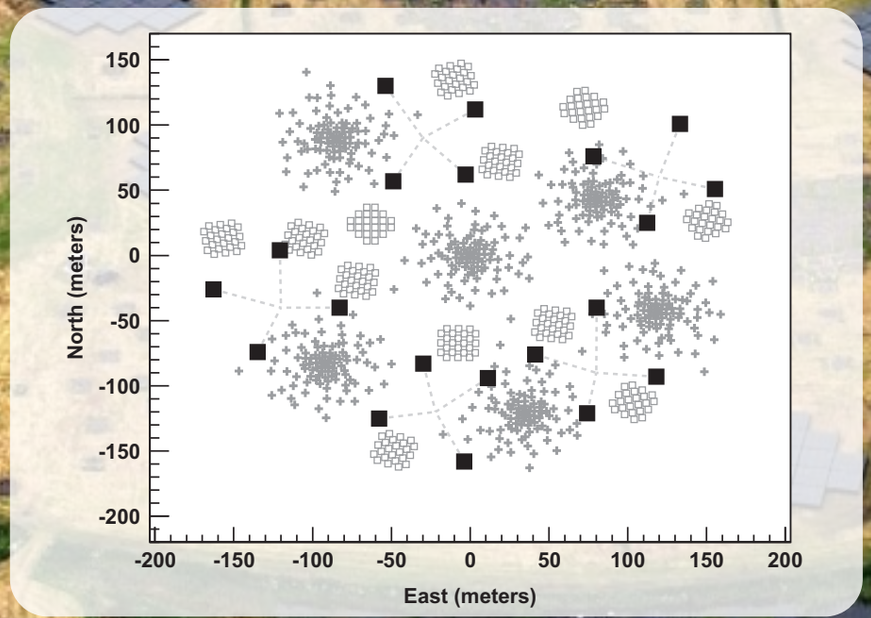

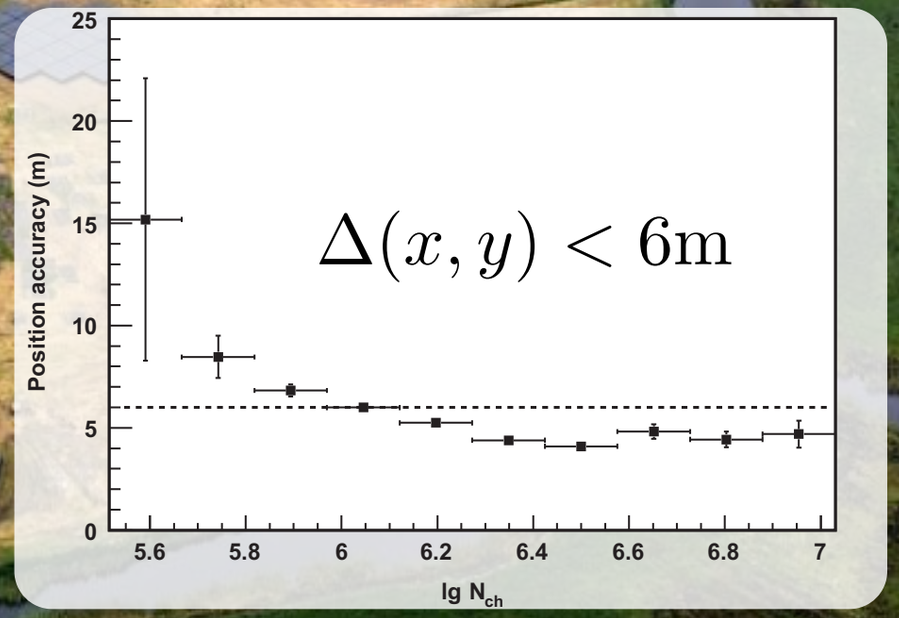

S. Thoudam et al, Nucl. Instr. Meth. A 767 (2014)

GRAPES experiment Ooty, India

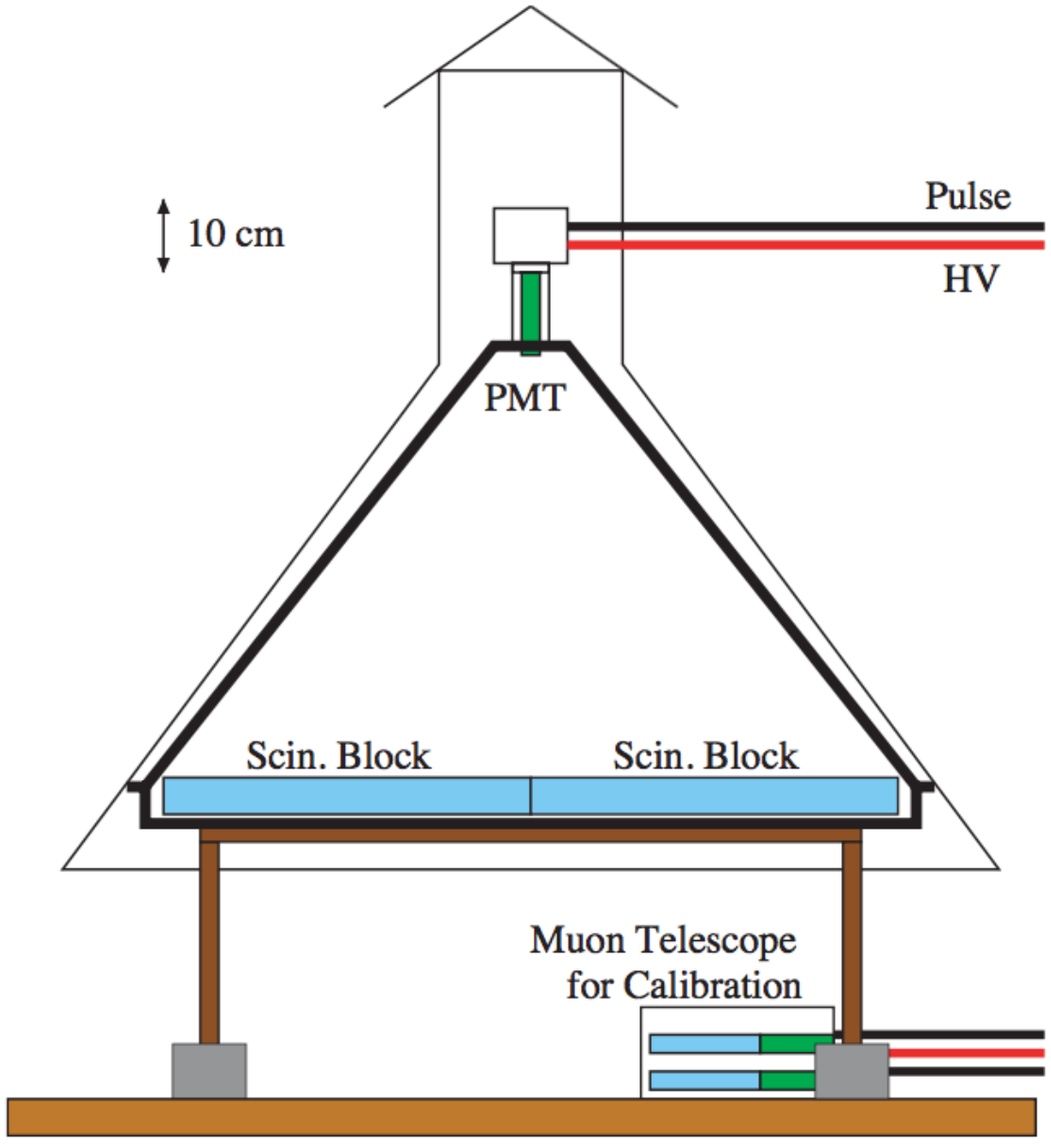

Fig. 3. Schematic of a shower detector, including the muon telescope under the detector, used for calibration.

Fig. 2. A view of the GRAPES-3 array showing electron detectors and the central control room. Four halls housing the muon detectors are seen on the left. The detectors lined up from the top-right to the bottom-left in the picture, are along the East to West direction.

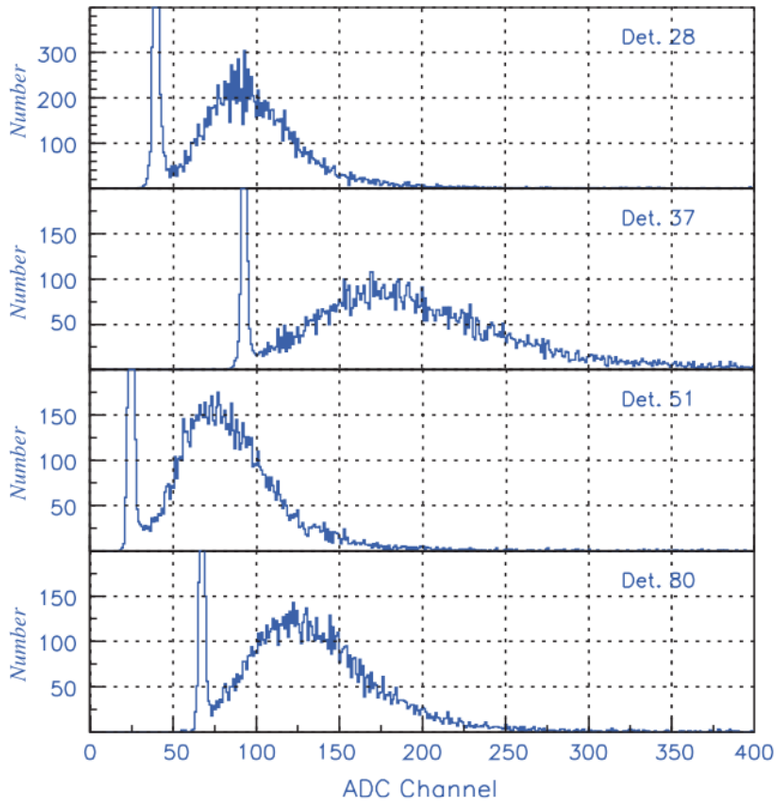

Fig. 4. Typical distributions of the integrated-charge (ADC value) for single particles (muons) for 4 shower detectors.

S.K. Gupta et al. / Nuclear Instruments and Methods in Physics Research A 540 (2005) 311–323

upgrade of Pierre Auger Observatory

SSD: surface scintillation detector

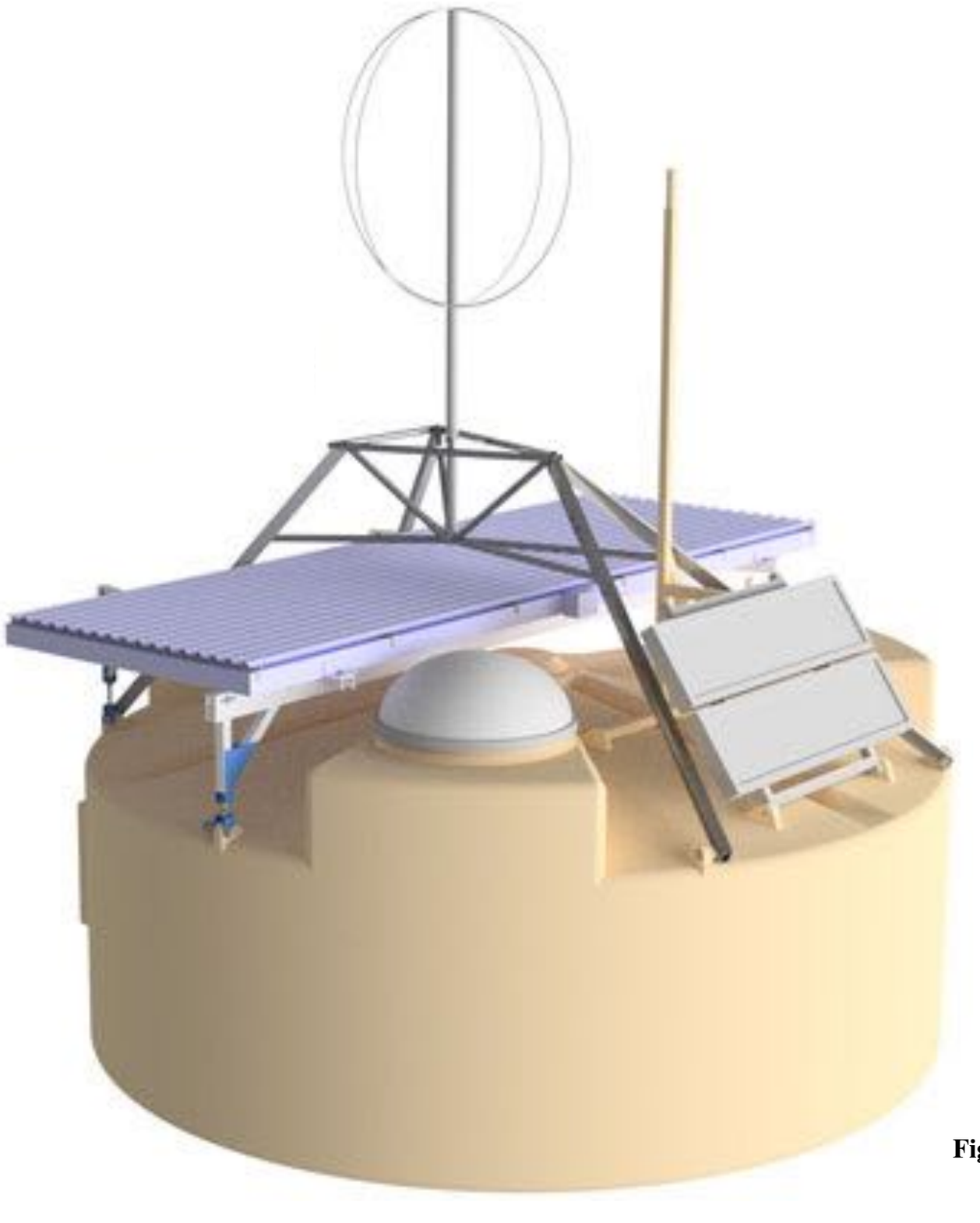

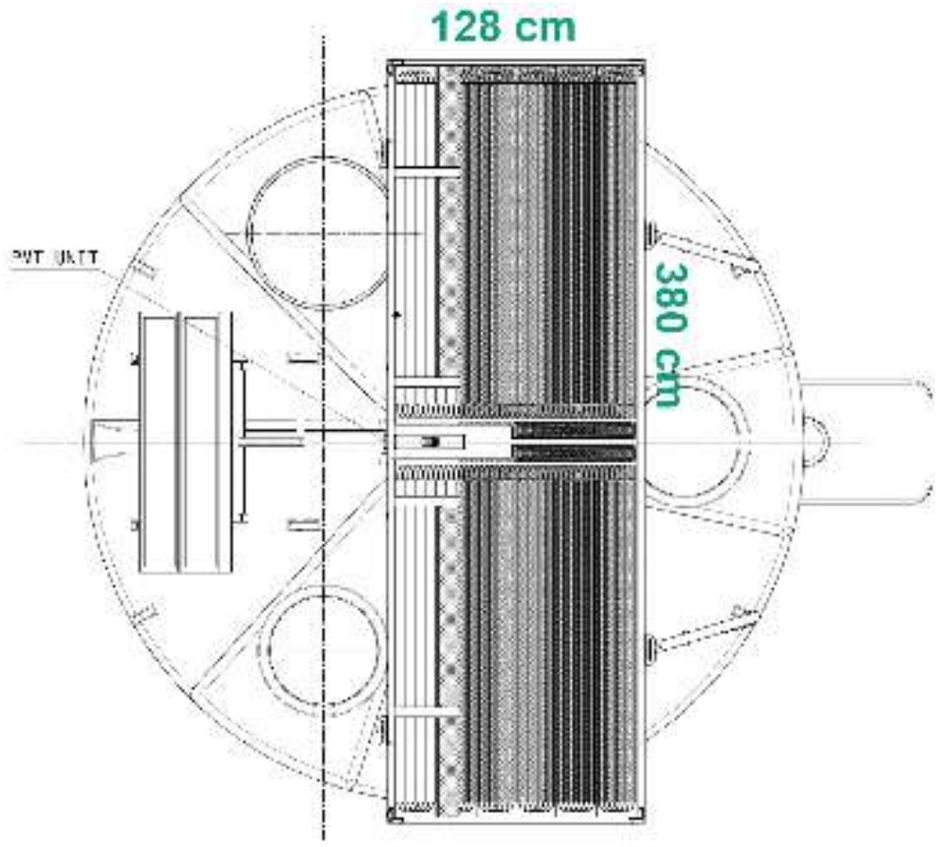

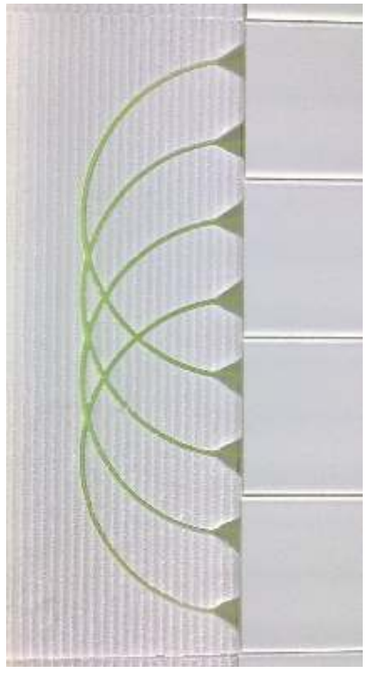

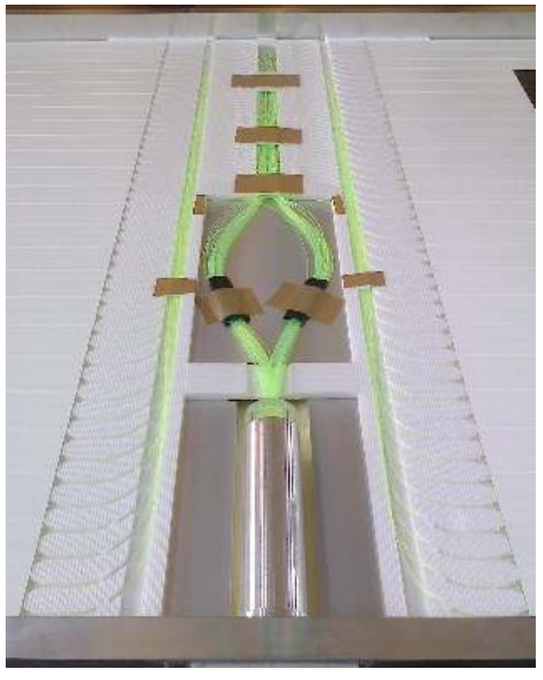

Figure 3: Routers for guiding and protecting fibers on the side *(left)* and in the center *(right)*.

upgrade of Pierre Auger Observatory

SSD: surface scintillation detector

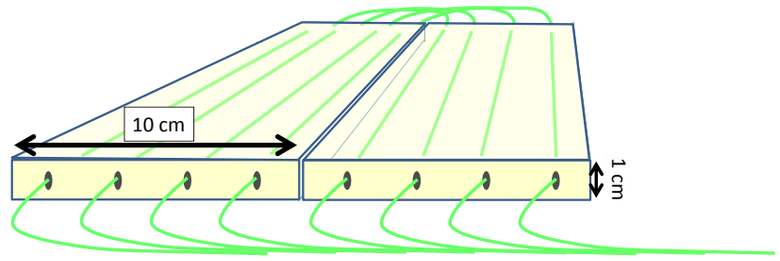

extruded plastic scintillator
read out by wavelength shifting fibers

Figure 4.2: Sketch view of bars with the fiber readout.

scintillator bars coated with TiO_2 outer layer for reflectivity

Kuraray Y11 WLS multi-clad optical fiber
1mm diamater

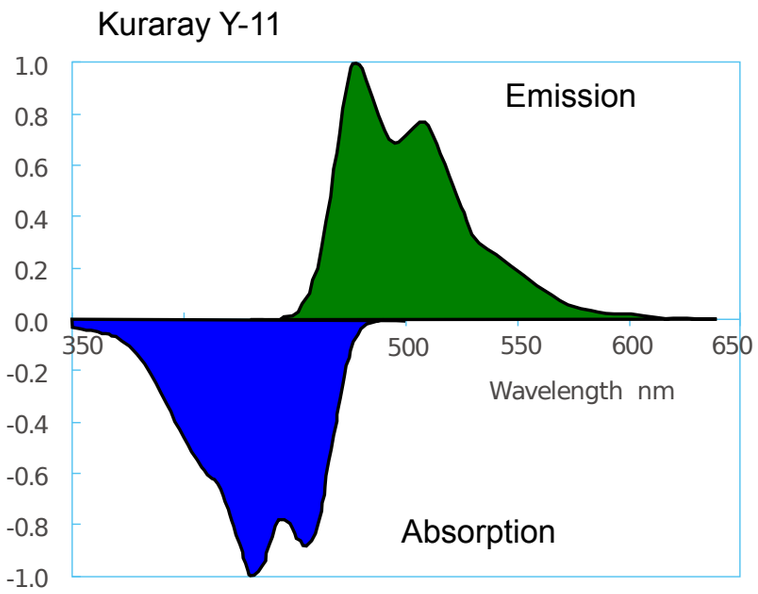

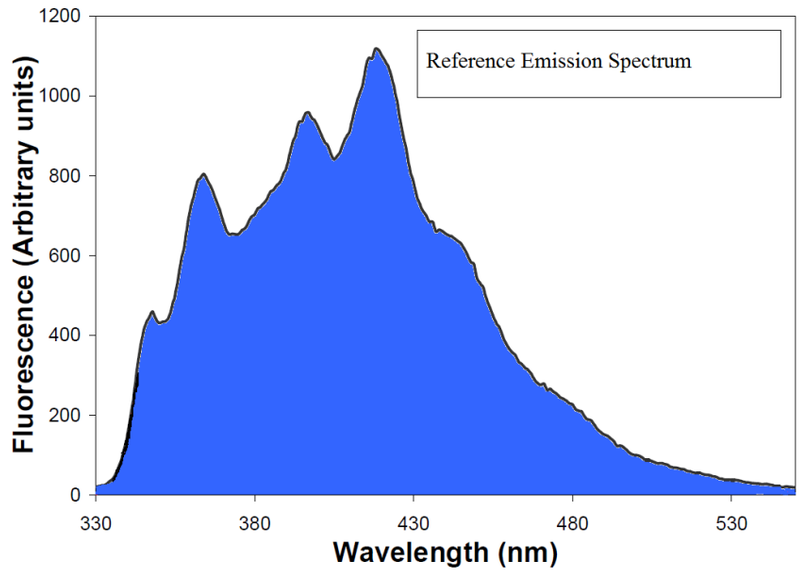

Figure 4.3: Left: emission and absorption spectra for Kuraray Y11 WLS fiber. Right: Reference emission spectrum of the chosen extruded scintillator.

upgrade of Pierre Auger Observatory

SSD: surface scintillation detector

4.2.3 PMTs and HV power supply

The baseline SSD photomultiplier is the Hamamatsu R9420, head-on type, 8-stage PMT with a 38 mm bialkali photocathode. This PMT shows good quantum efficiency at the wavelength of interest (in the green region) associated with an excellent linearity range (when the PMT is supplied through a tapered ratio divider) of up to 200 mA of peak anode current for an operating gain of 7×10^5 (Figure 4.9). As an alternative, the performance of the lower cost Hamamatsu R8619 PMT is being investigated.

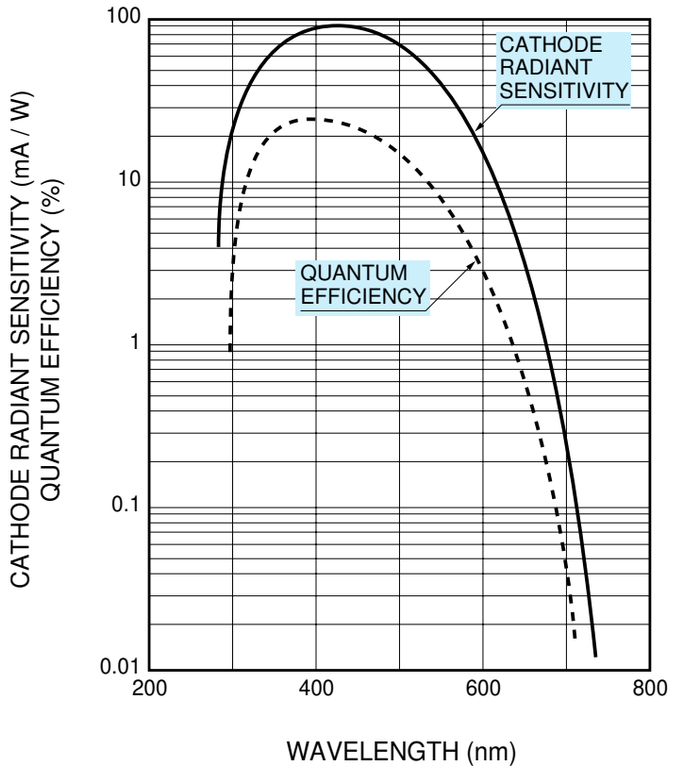

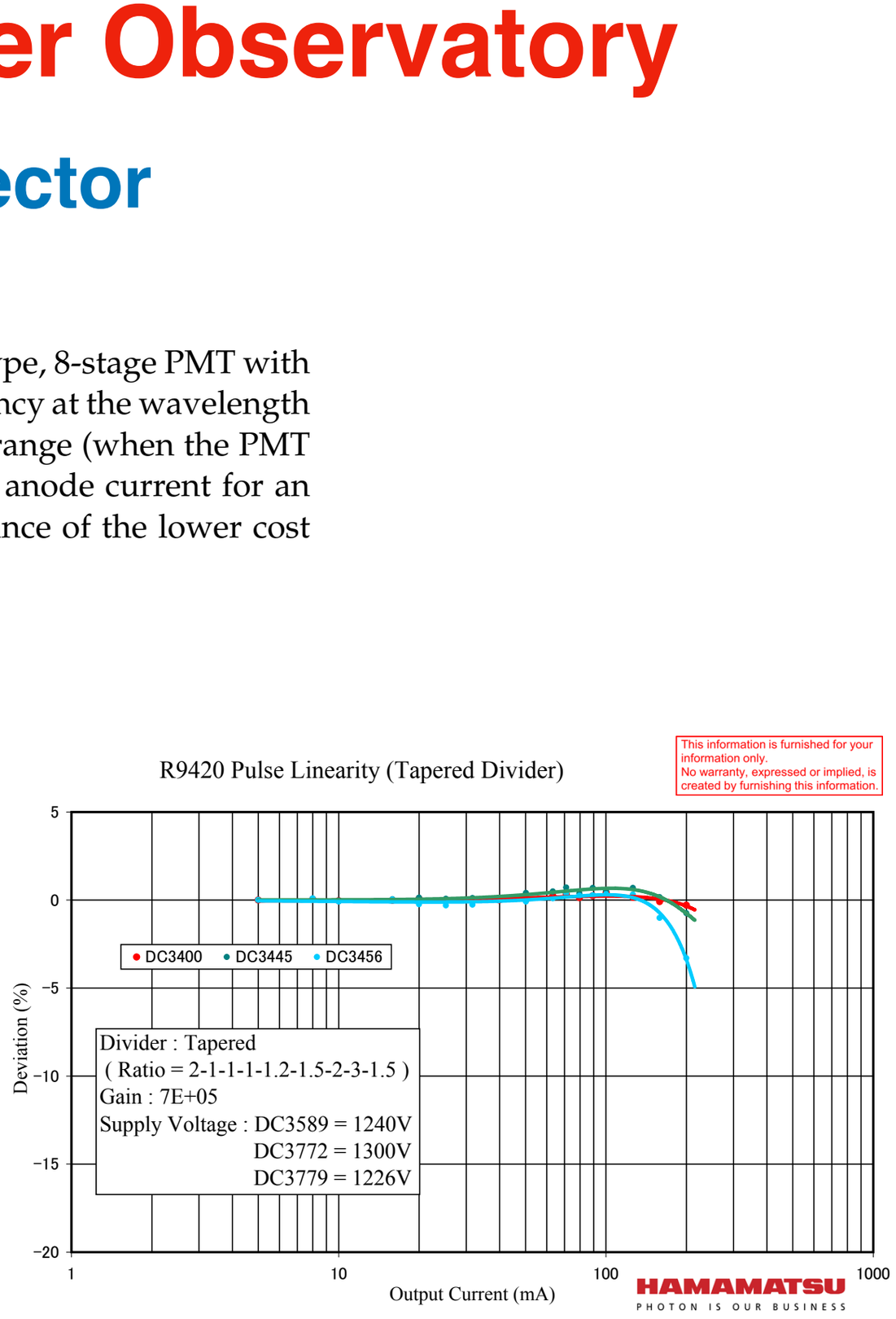

Figure 4.9: Top: Hamamatsu R9420 quantum efficiency. Bottom: Hamamatsu R9420 linearity.

upgrade of Pierre Auger Observatory

SSD: surface scintillation detector

production at RU Nijmegen

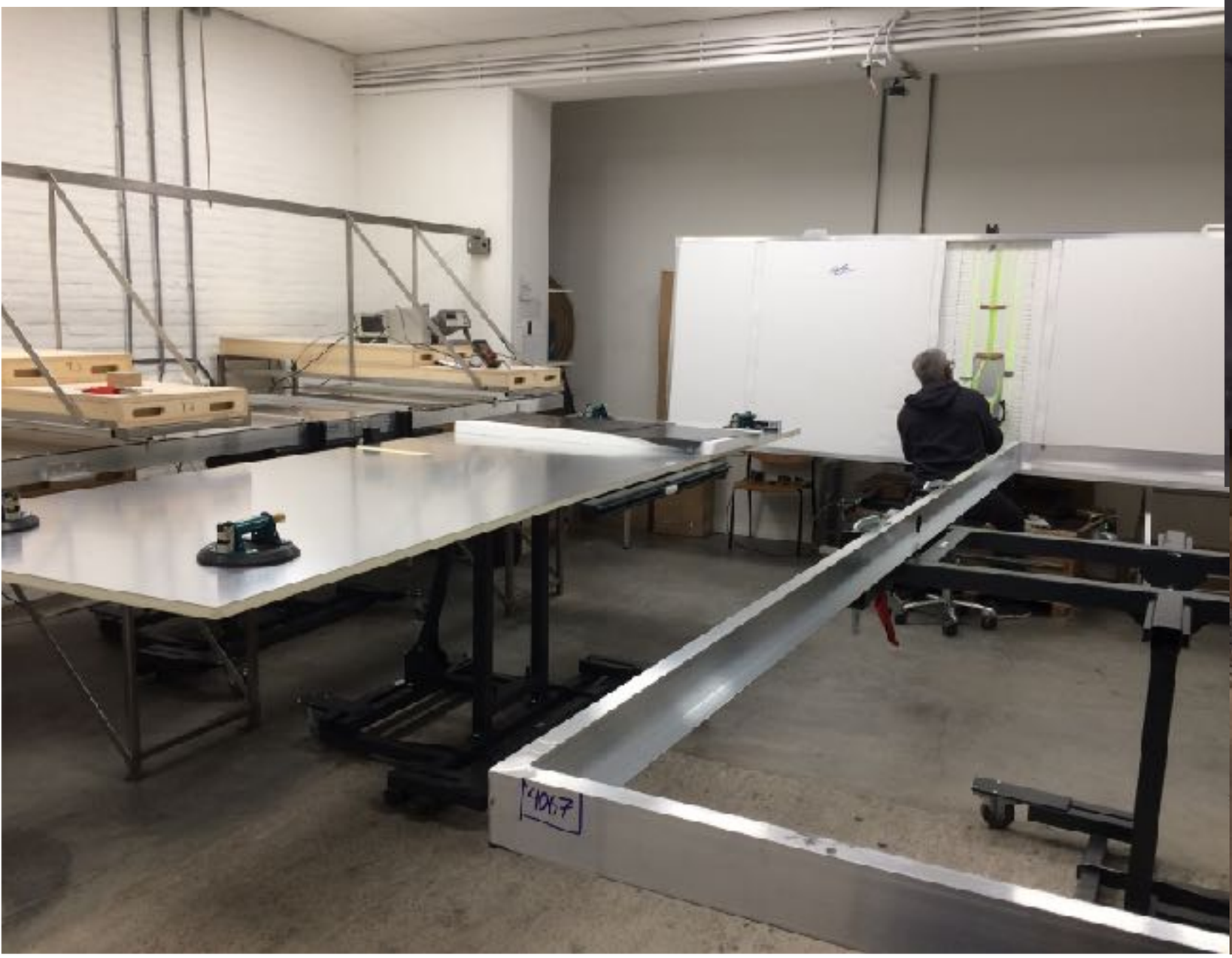

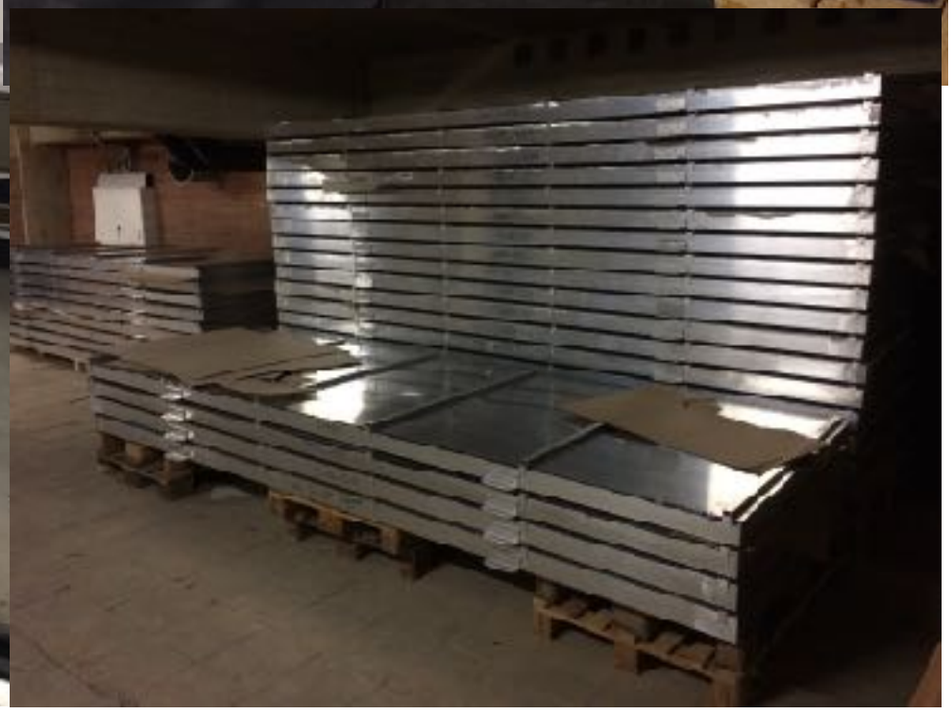

Avalanche Photo Diode - APD
Silicon Photo Multiplier - SiPM

HAMAMATSU
PHOTON IS OUR BUSINESS

Silicon Photomultiplier

Operation, Performance & Possible Applications

Slawomir Piatek

Technical Consultant, Hamamatsu Corp.

HAMAMATSU
PHOTON IS OUR BUSINESS

Introduction

Very high intrinsic gain together with minimal excess noise make silicon photomultiplier (SiPM) a possible choice of a photodetector in those applications where the input light is in the photon-counting range.

SiPM

Structure and Operation of a SiPM

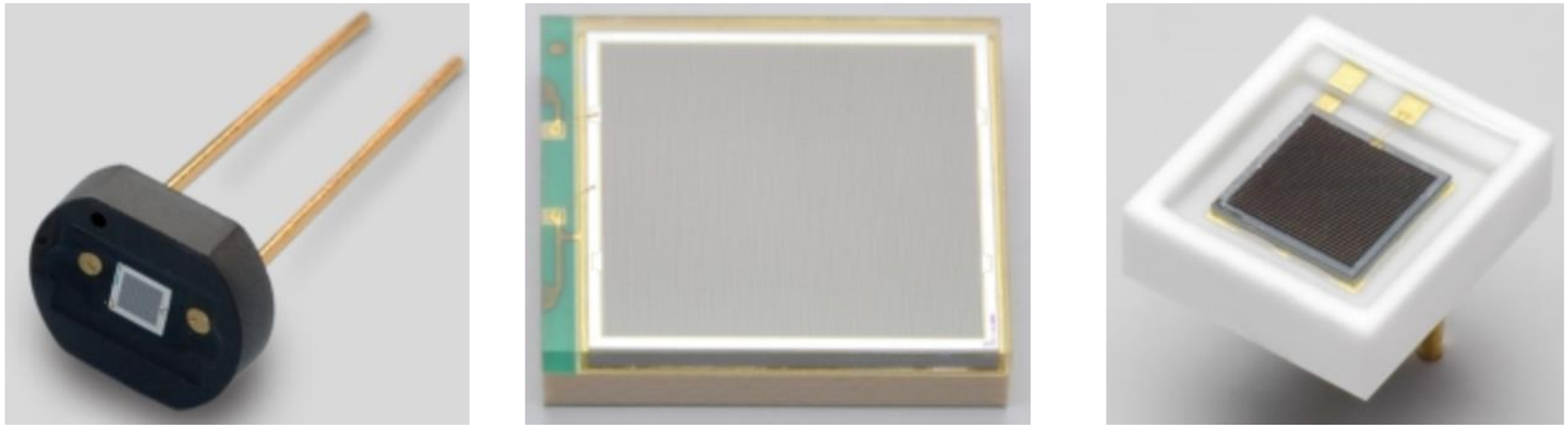

Portraits of SiPMs (images not to scale)

SiPM structure

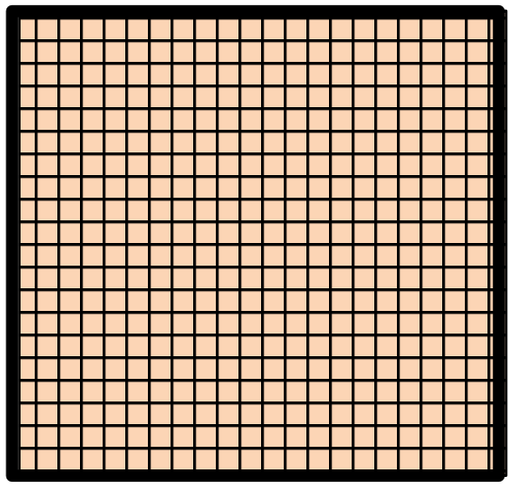

SiPM is an array of microcells

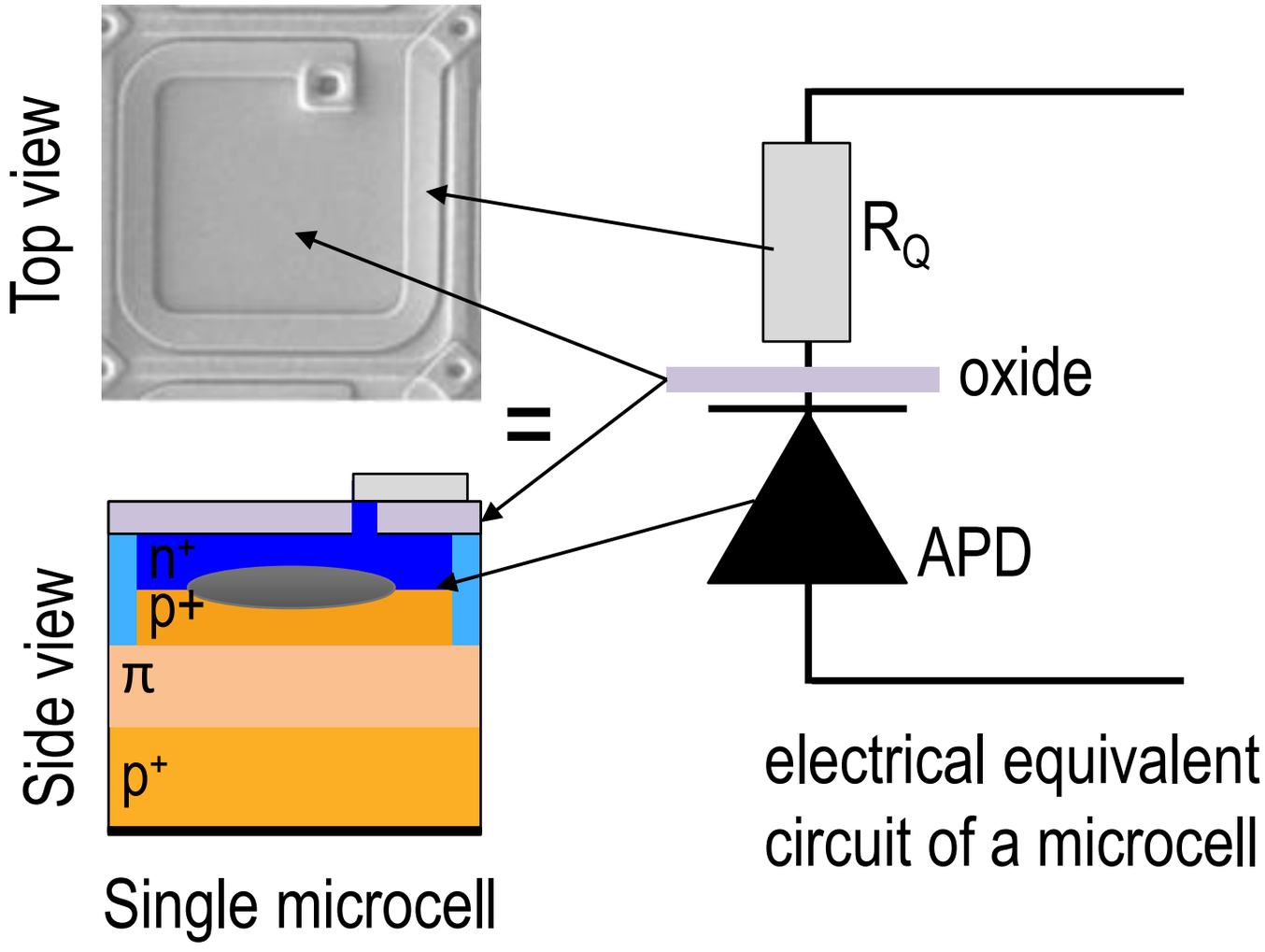

SiPM structure

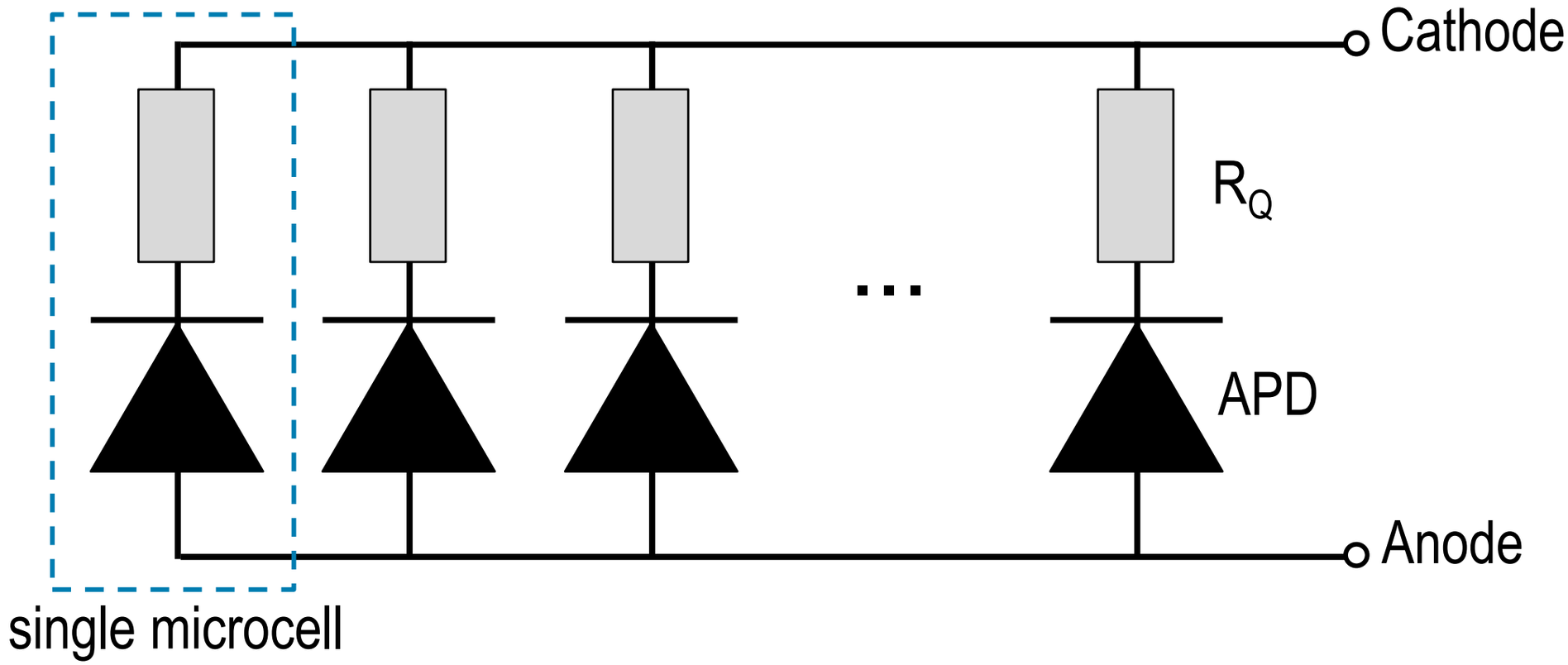

All of the microcells are connected in parallel

SiPM specifications

Active area: 1.3×1.3 – 6×6 mm^2

Microcell size (pitch): 10×10, 15×15, 25×25, 50×50, 75×75 μm^2

Number of microcells: (active area)/(microcell size), from 100's to 10,000's

Overvoltage: $\Delta V = V_{BIAS} - V_{BD}$; recommended by the manufacturer

SiPM operation

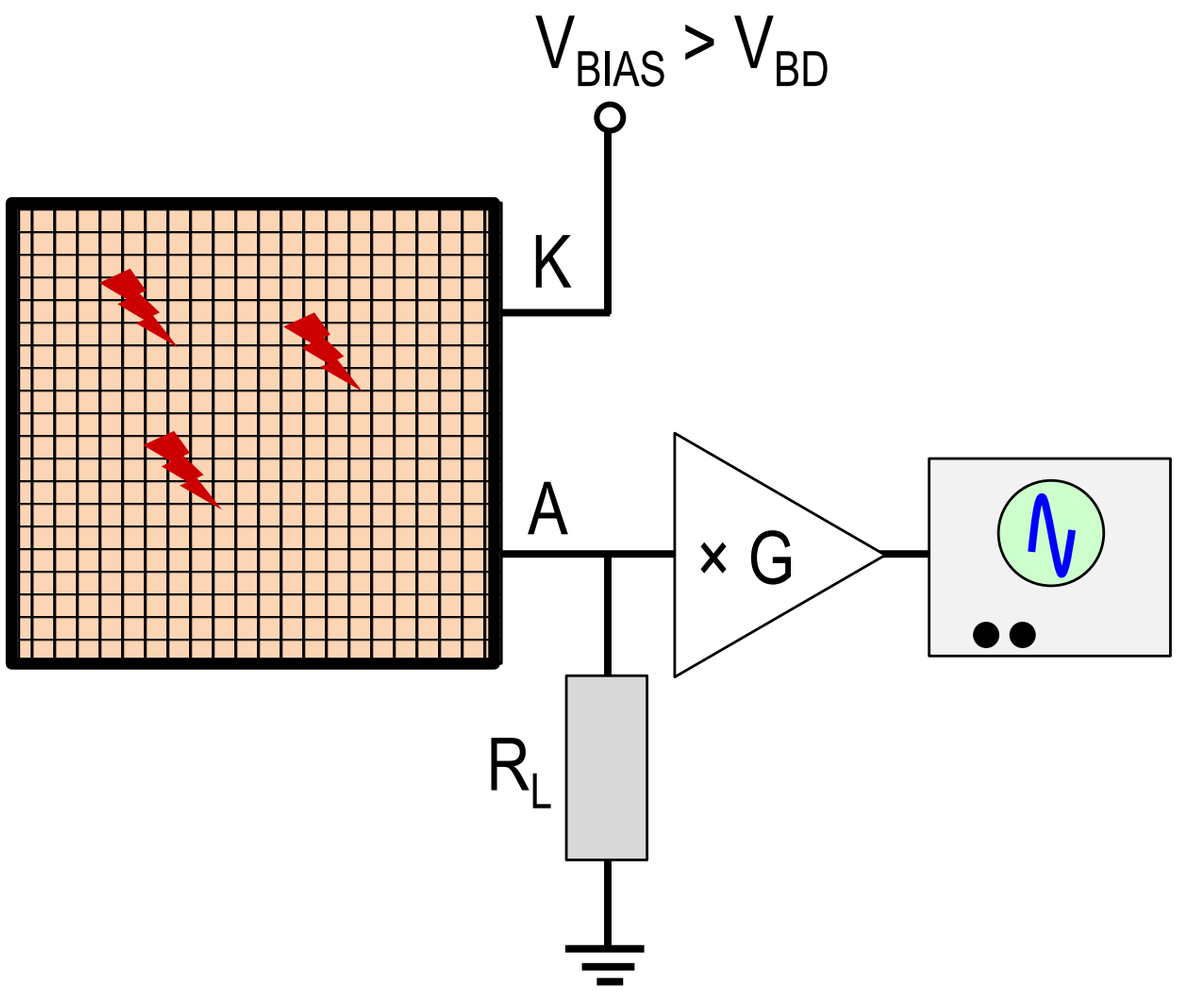

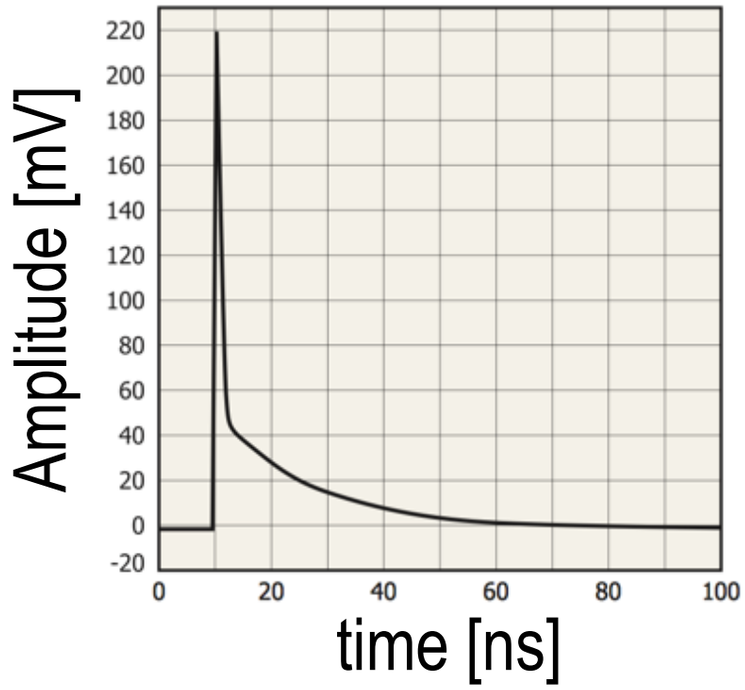

Example of single-photoelectron waveform (1 p.e.)

Gain = area under the curve in electrons

SiPM operation

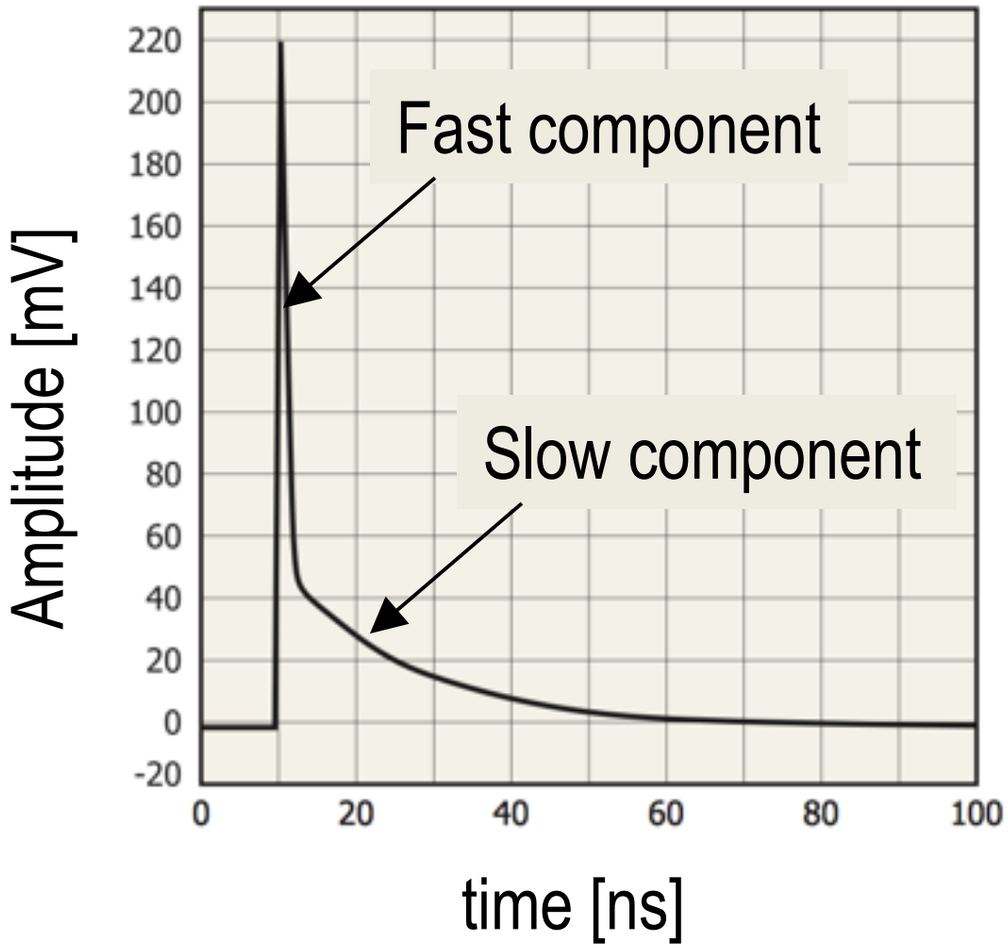

RC time constant of the slow component depends on microcell size (all else being equal)

Recovery time $t_R \approx 5$ times the RC time constant

t_R is on the order of 10's to 100's ns but in practical situations, it is also a function of detection bandwidth

HAMAMATSU
PHOTON IS OUR BUSINESS

SiPM operation

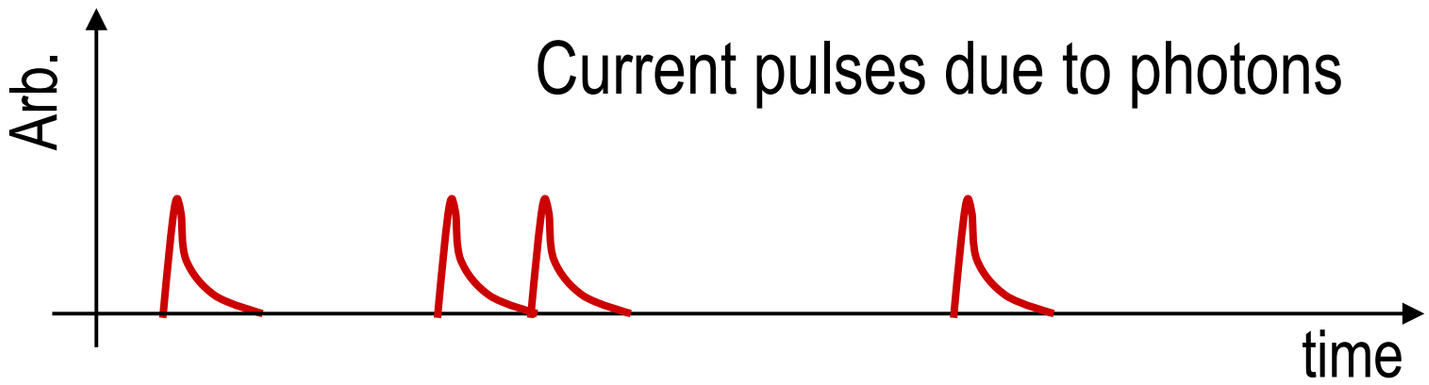

The output of an SiPM is a chronological superposition of current pulses

SiPM also outputs current pulses even in absence of light: dark counts (dark current)

Dark Counts

Current pulses due to photons and dark counts are indistinguishable

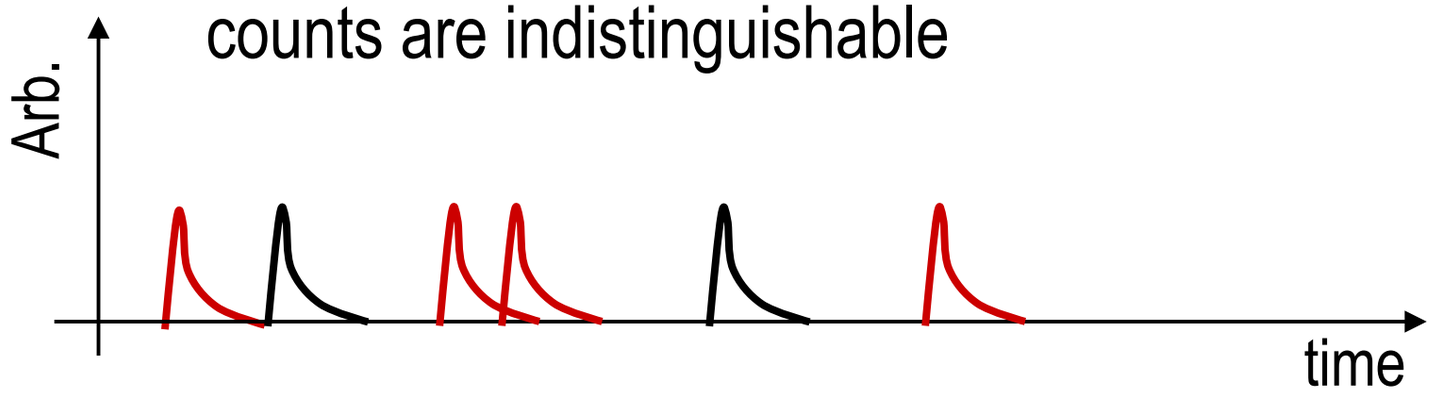

Dark-count pulses are indistinguishable from those due to photons

The rate of dark counts depends on overvoltage, temperature, and size of the active area

Crosstalk

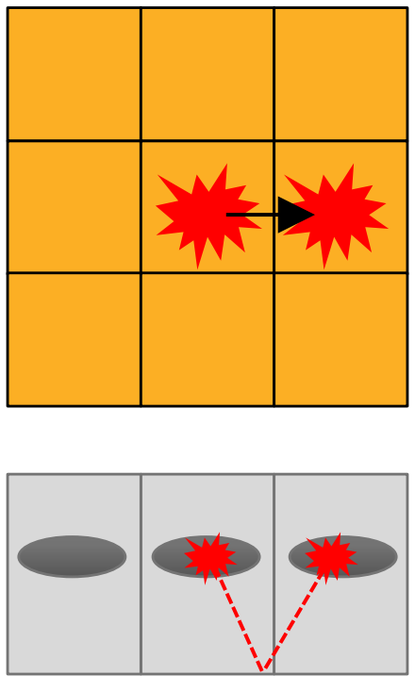

Primary discharge can trigger a secondary discharge in neighboring microcells. This is crosstalk.

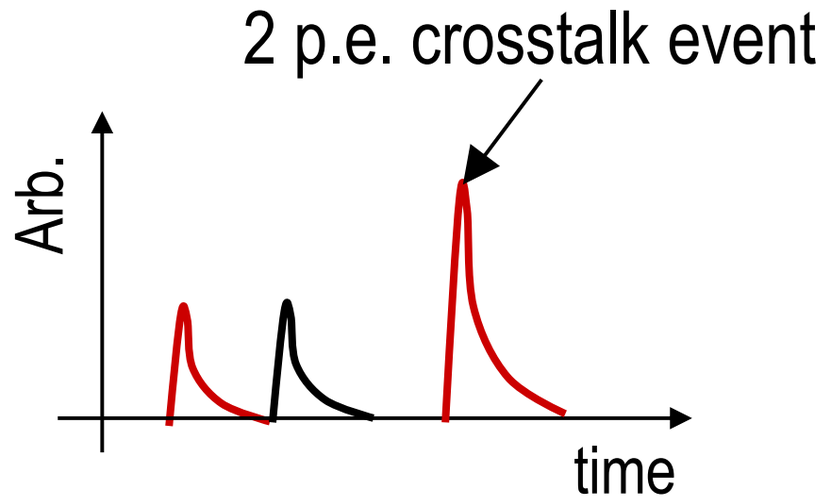

Crosstalk probability depends on overvoltage

Operation

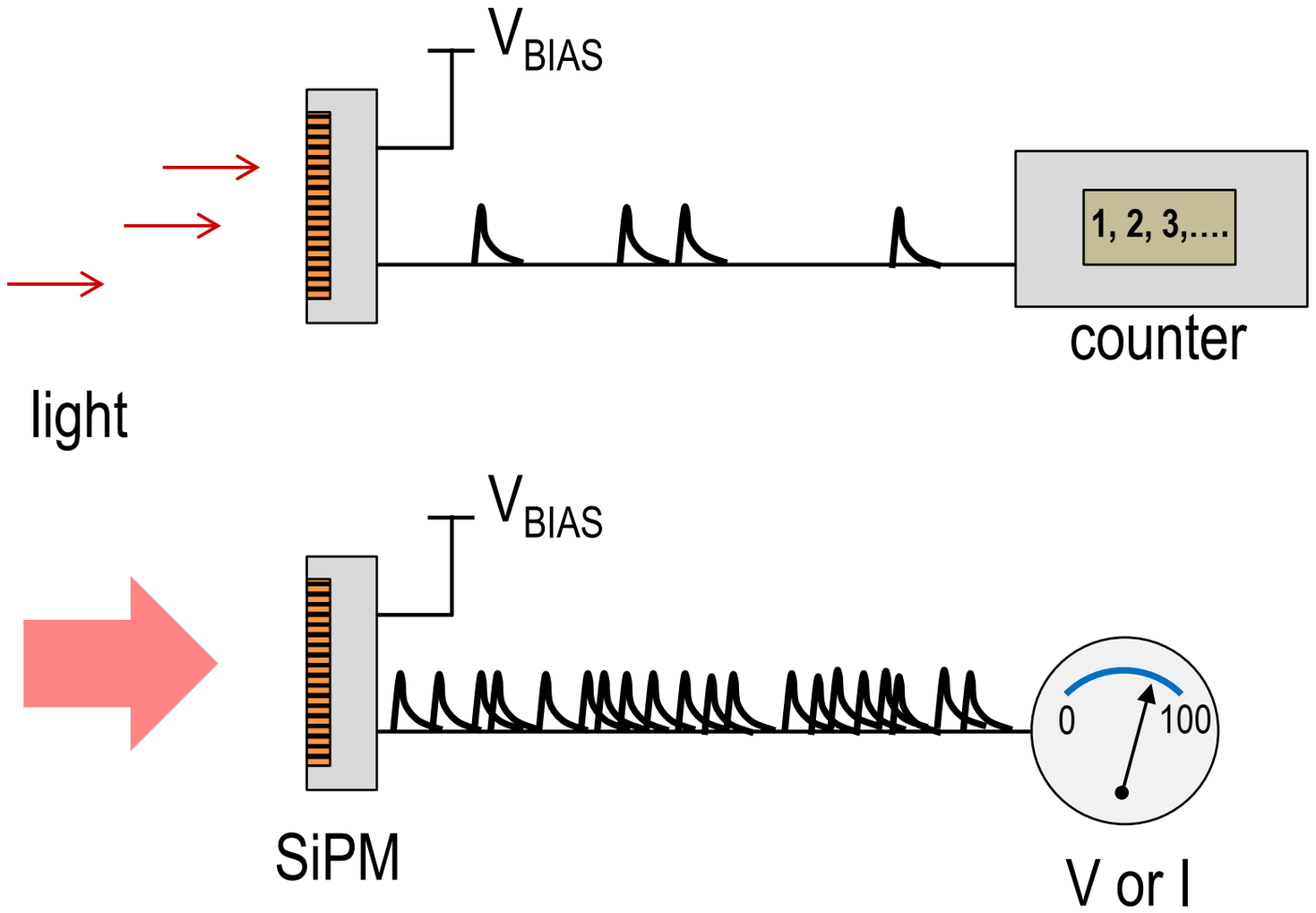

If the pulses are distinguishable, SiPM can be operated in a **photon counting** mode.

If the pulses overlap, the SiPM can be operated in an **analog mode**. The measured output is voltage or current.

SiPM *detection circuits*

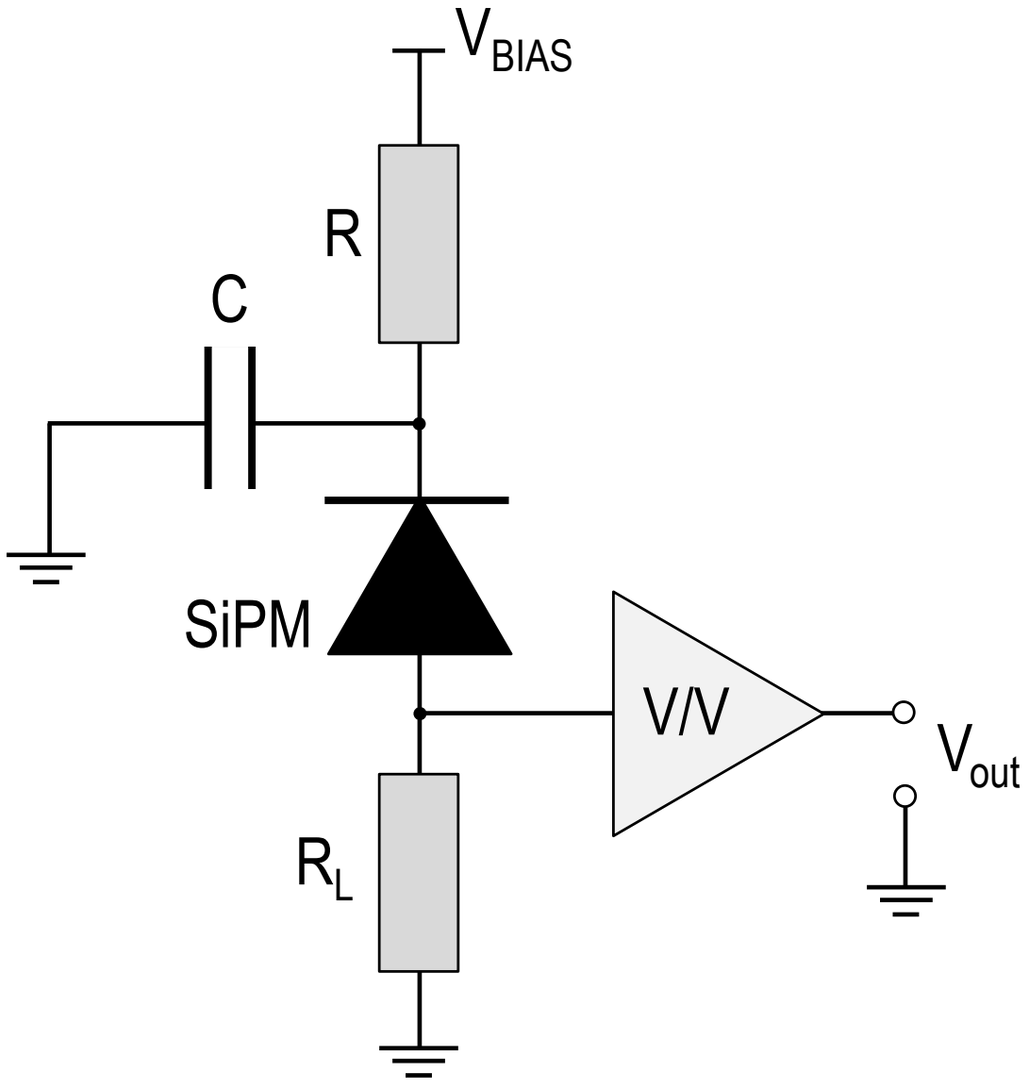

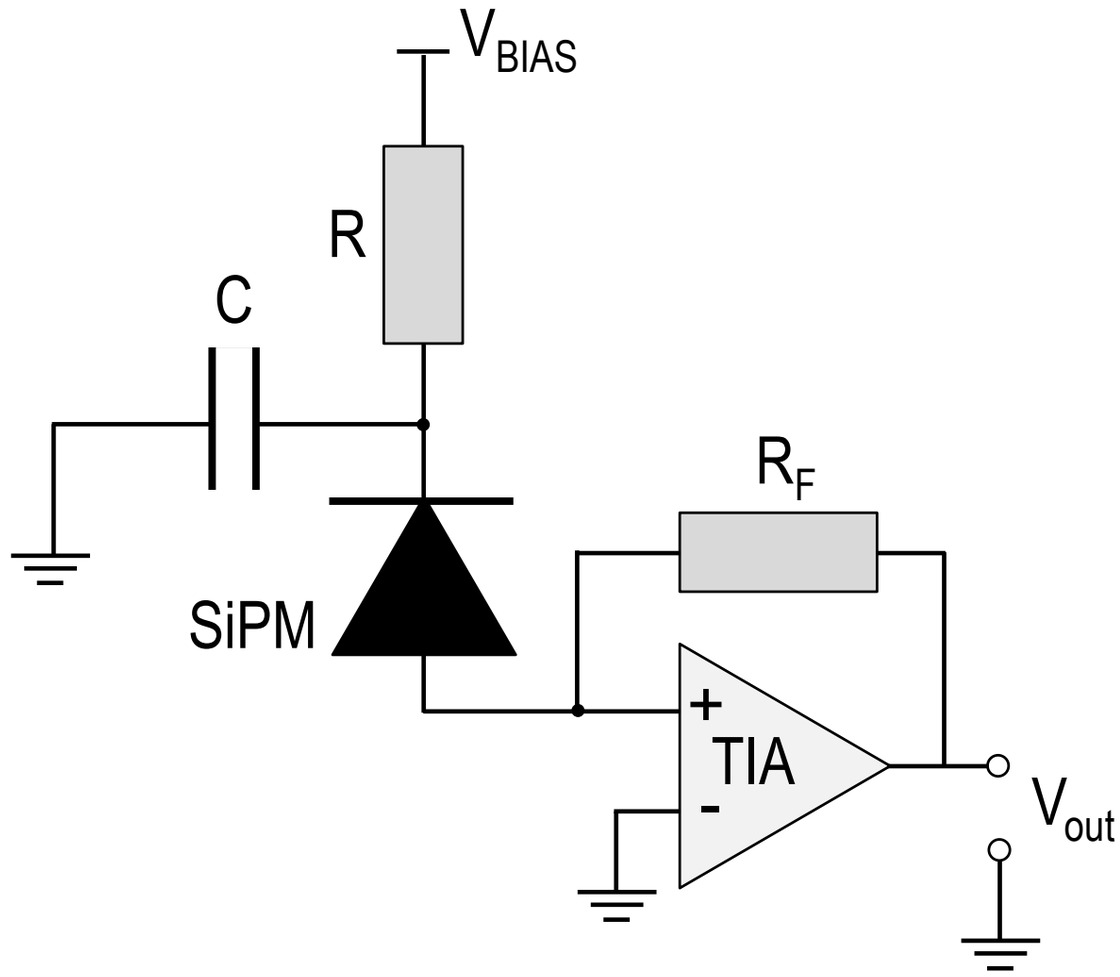

HAMAMATSU
PHOTON IS OUR BUSINESS

Characteristics of a SiPM

- Photon detection efficiency
- Gain
- Temperature effects
- Crosstalk probability
- Dark current & dark counts
- Linearity & dynamic range

Photon detection efficiency

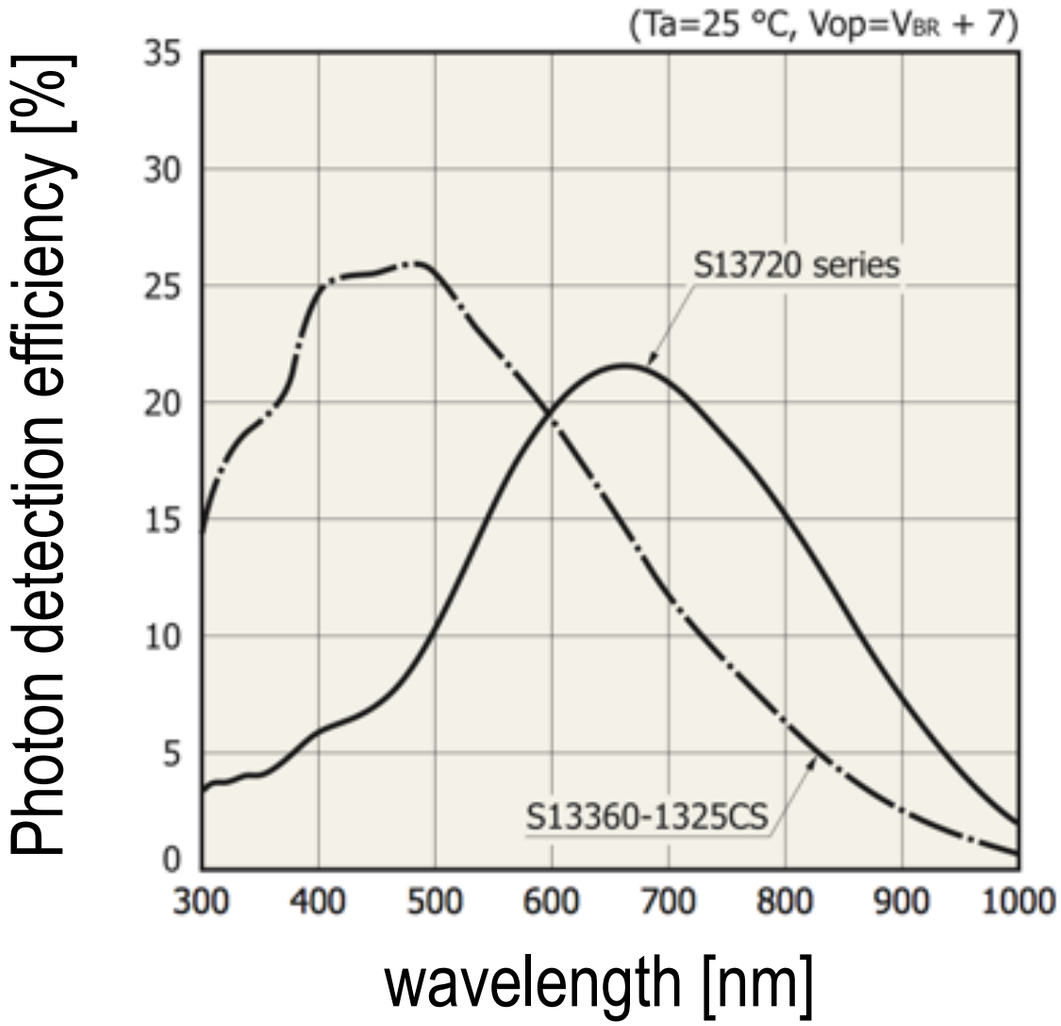

- Photon detection efficiency (PDE) is a probability that an incident photon is detected. It depends on:
  - wavelength
  - overvoltage
  - microcell size

Peak PDE 20% – 50%

Photon detection efficiency

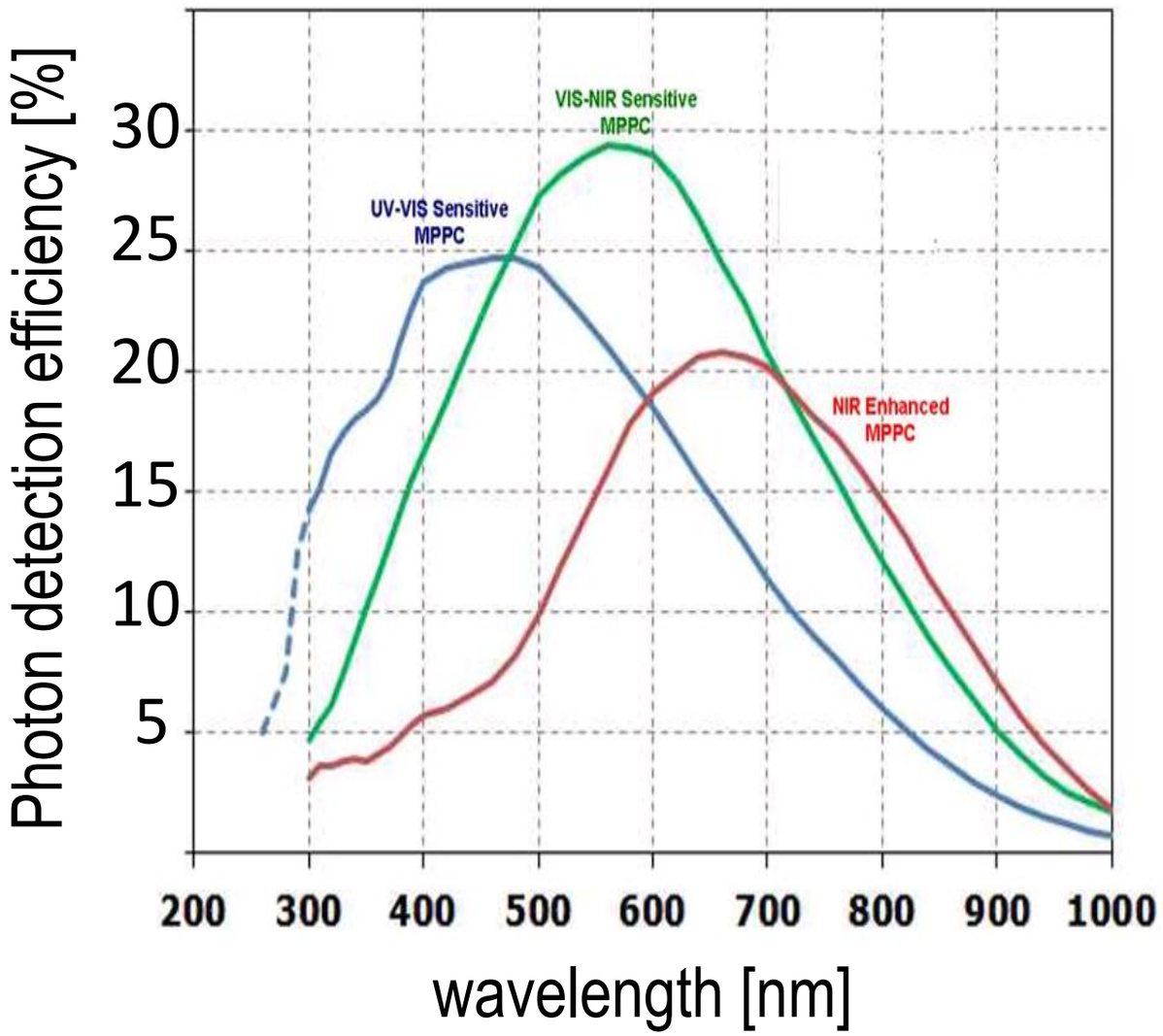

Examples of PDE curves for SiPMs optimized for NIR, VIS, and UV response.

Gain

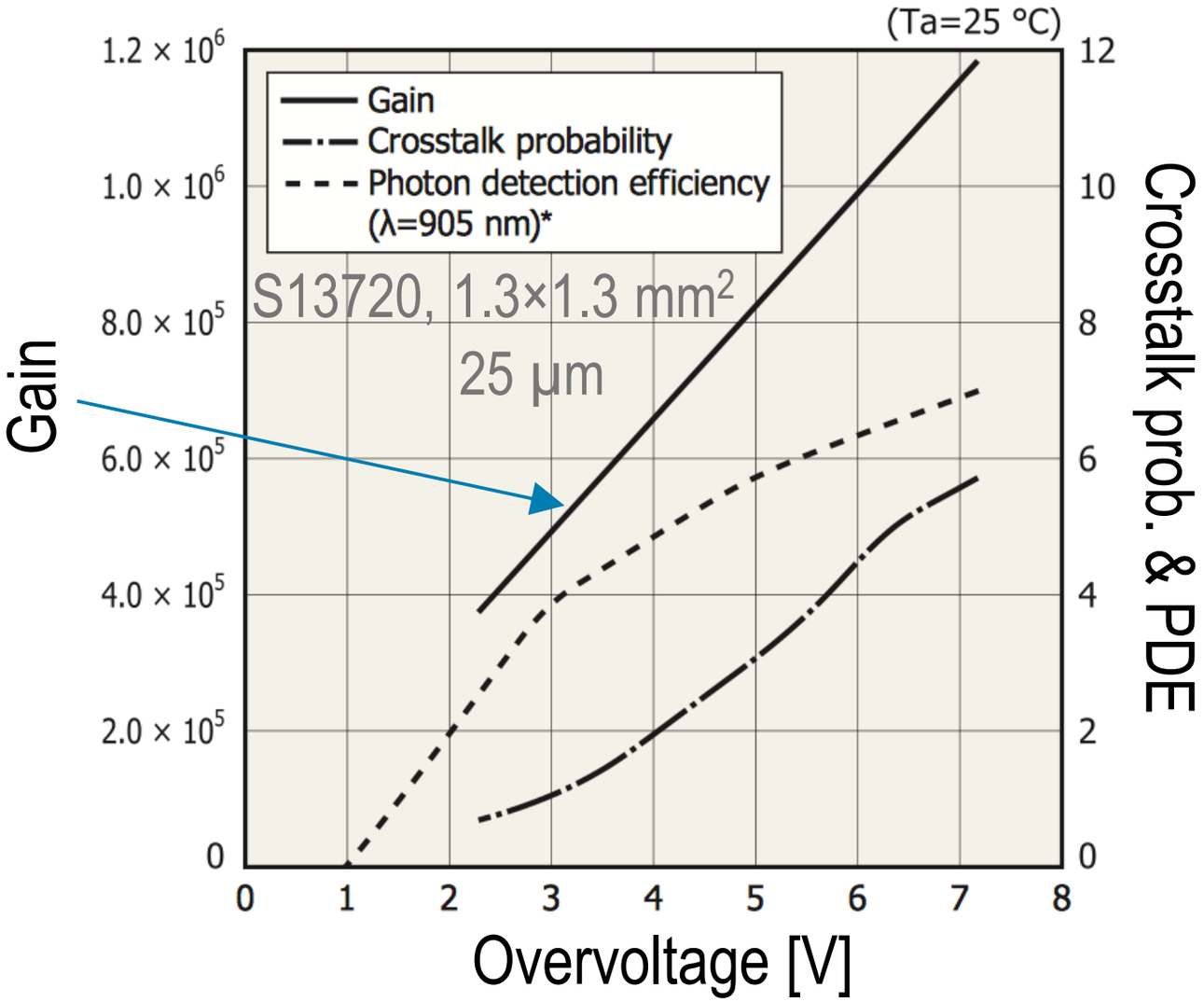

- Gain of SiPM is comparable to that of a PMT.

  Excess noise very low:
  F ~ 1.1, mostly due to crosstalk

- Gain depends linearly on overvoltage

Gain *versus* temperature

Does gain of an SiPM depend on temperature?

Yes – if the bias voltage is fixed

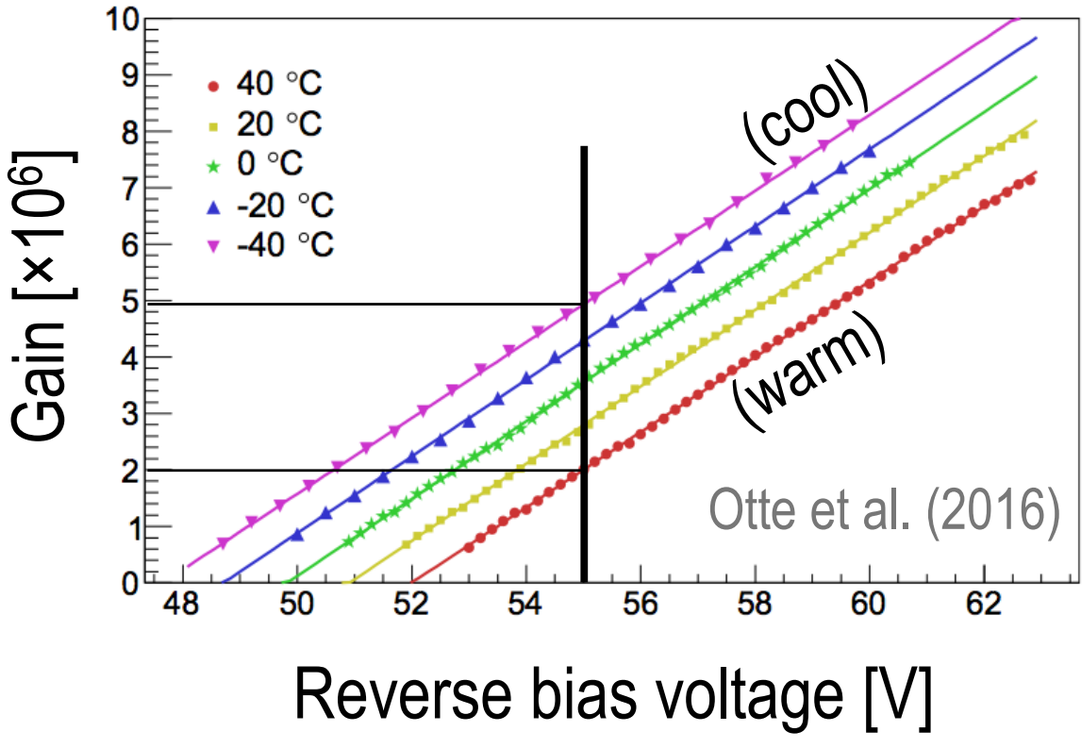

Gain *versus* temperature

Does gain of an SiPM depend on temperature?

No – if the overvoltage is fixed

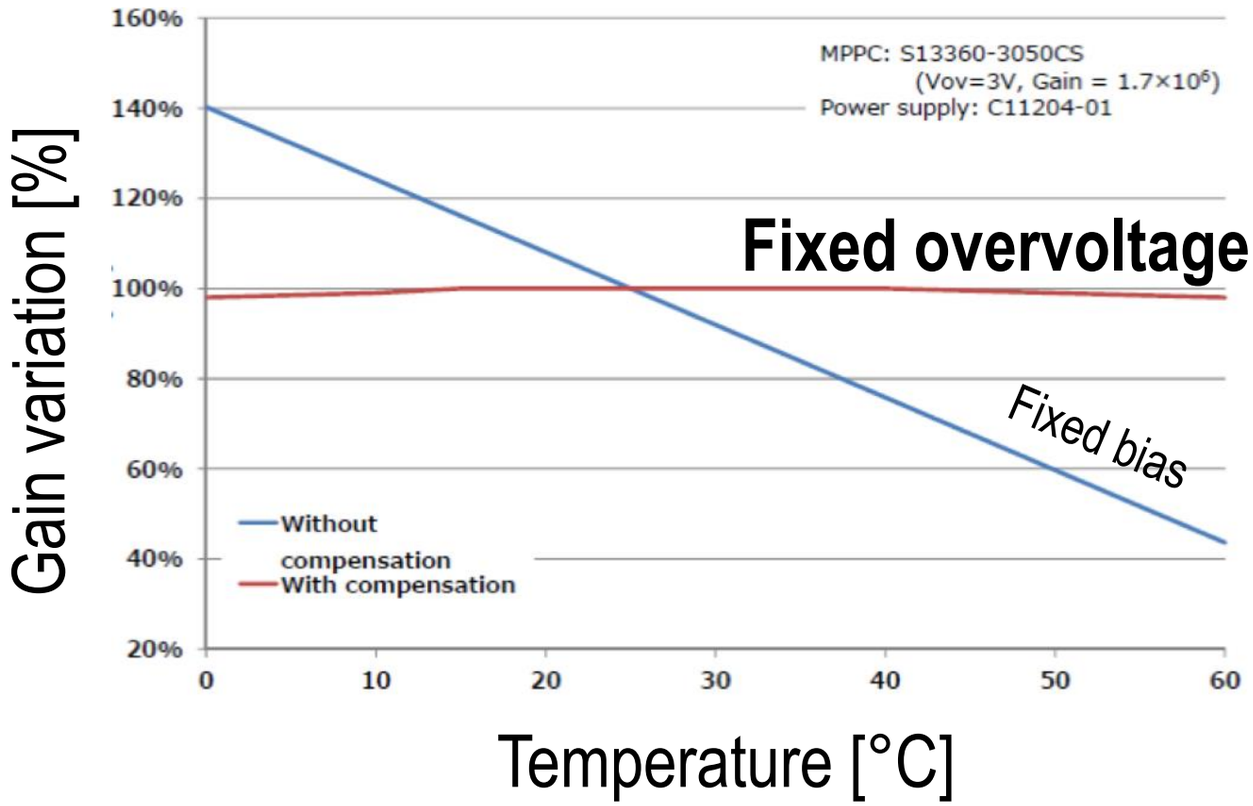

Crosstalk

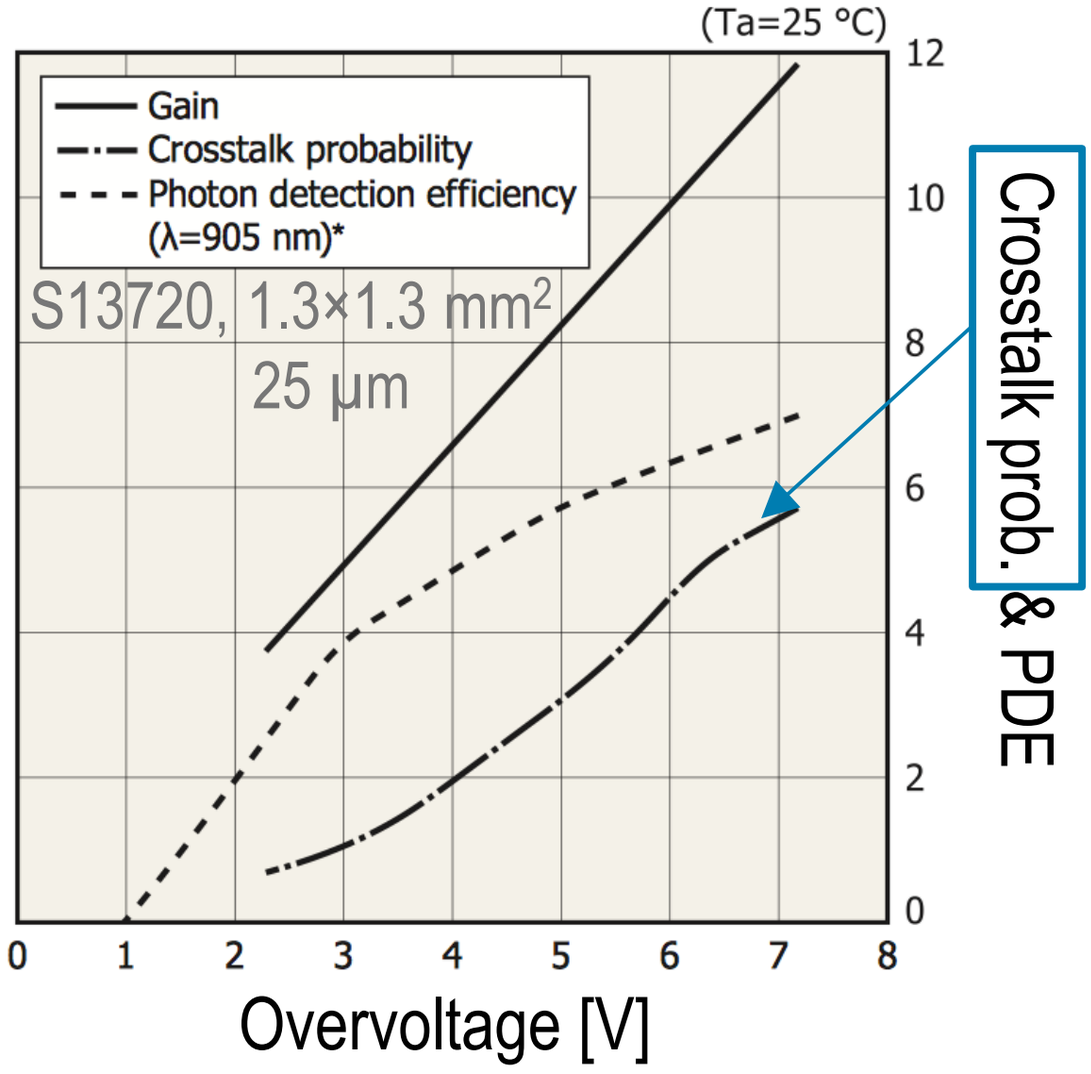

P_{CT} increases with overvoltage

Crosstalk is the main contributor to excess noise

$$F \approx (1+P_{CT})$$

Dark Current

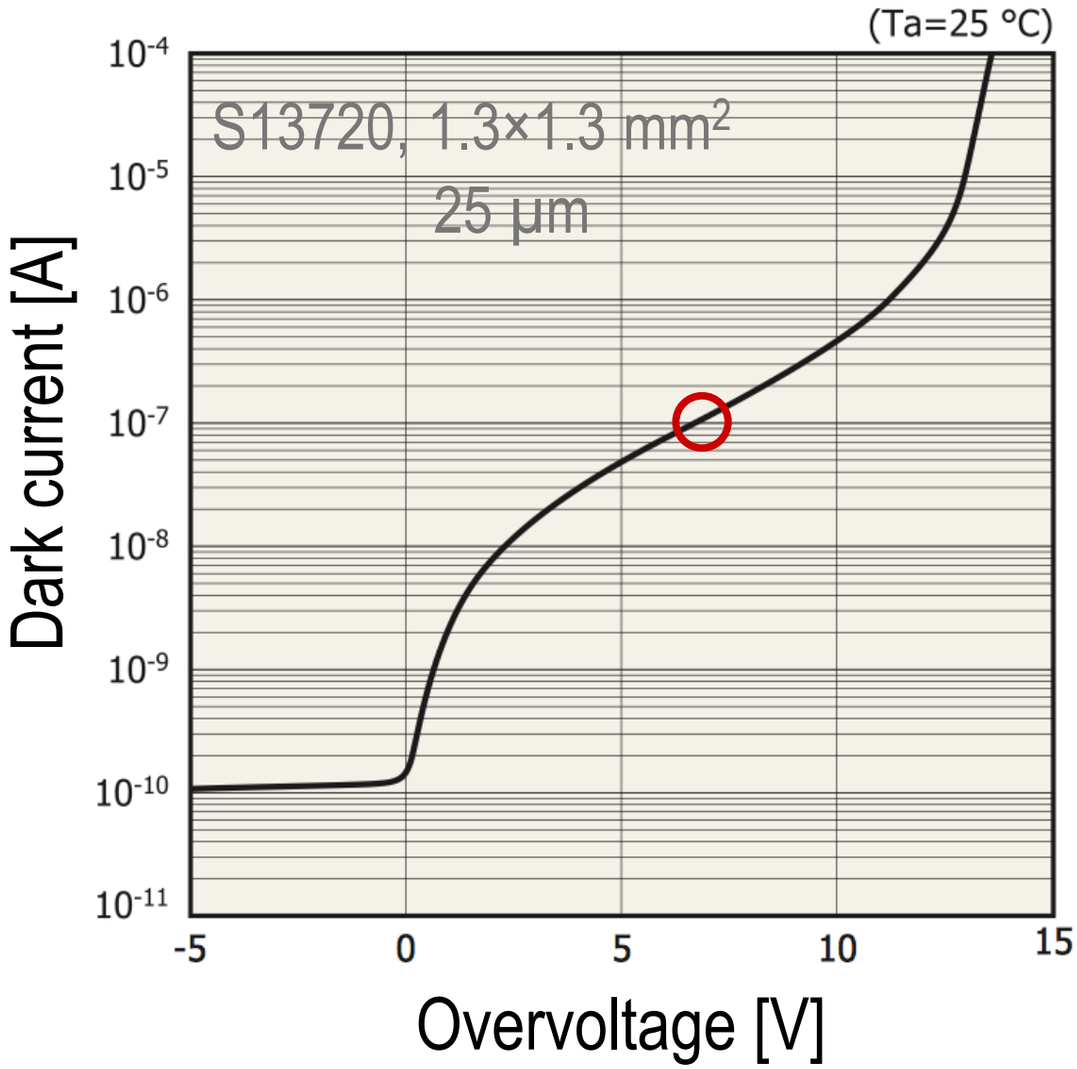

Example of dark current versus overvoltage

$$DCR = I_D/e\mu$$

$I_D = 1\times10^{-7}$ A (at 7 V)

$\mu = 1.2\times10^{6}$ (at 7 V)

-> DCR ≈ 520 kHz

or once per about 2 µs

Linearity and dynamic range

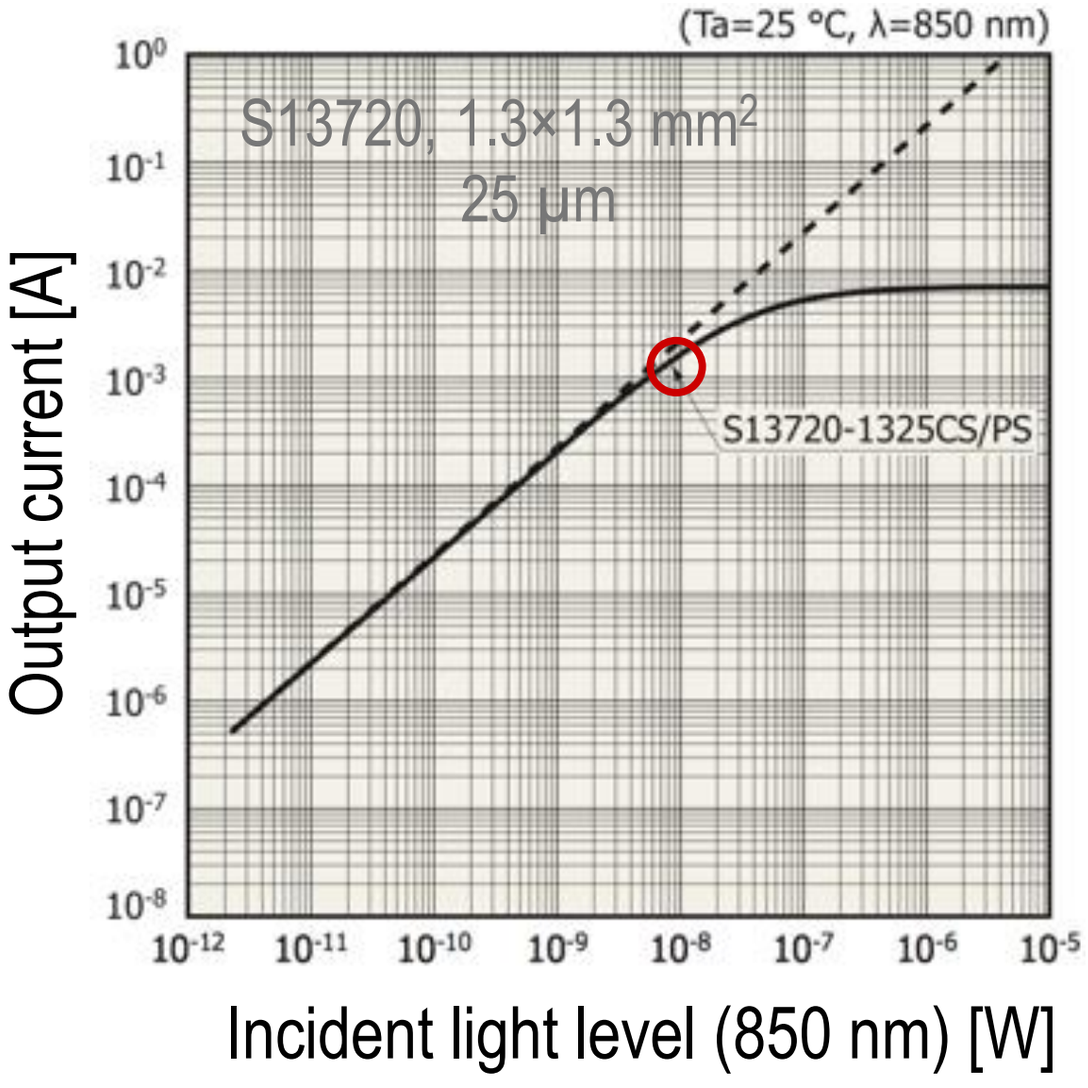

Example of output current versus incident light level.

Photon irradiance (at 850 nm) = $4.3\times10^{18}\times$ P[W]

P = 10^{-8} W –> 4.3×10^{10} photons per second

Linearity depends on the number of microcells for a given active area

HAMAMATSU
PHOTON IS OUR BUSINESS

SiPM, PMT & APD

This webinar will compare and contrast SiPM with a photomultiplier tube (PMT) and APD.

Let’s briefly review the operation of a PMT and APD

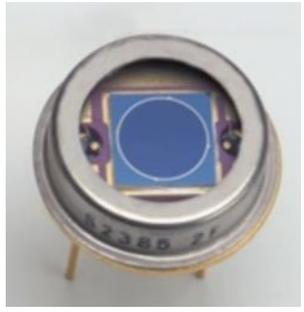

Examples of a PMT (left) and APD (right).

Operation of a PMT

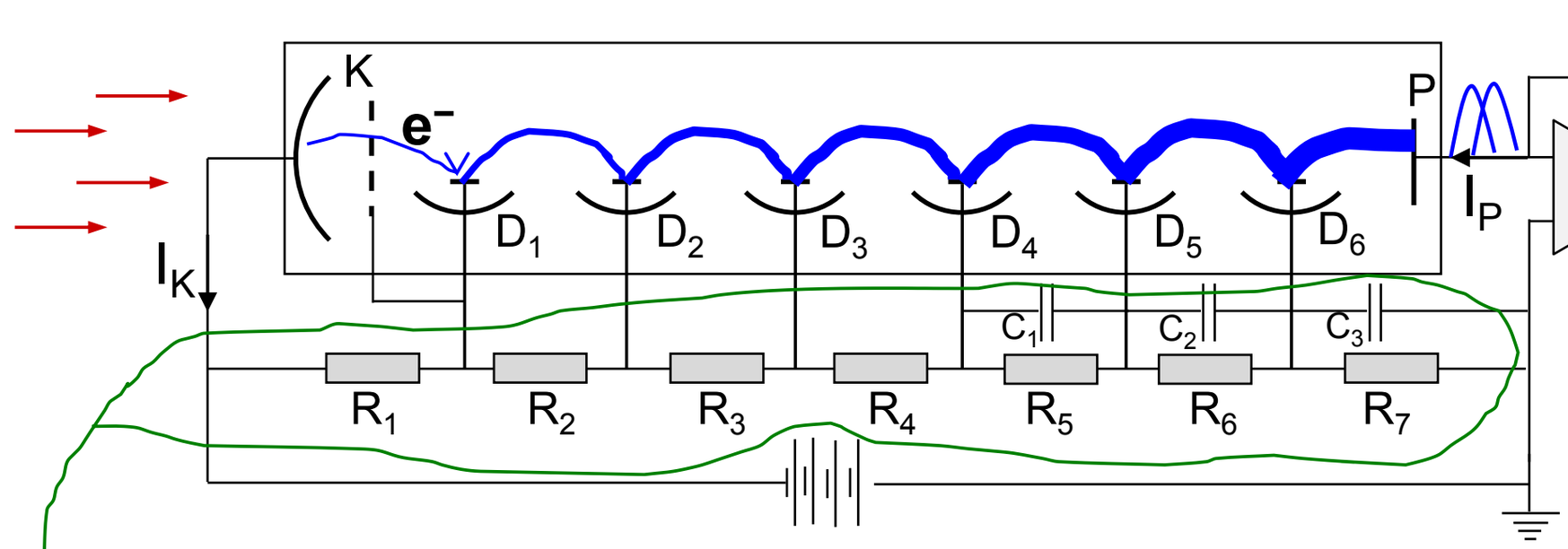

V ~ 1000 V

Typical voltage divider

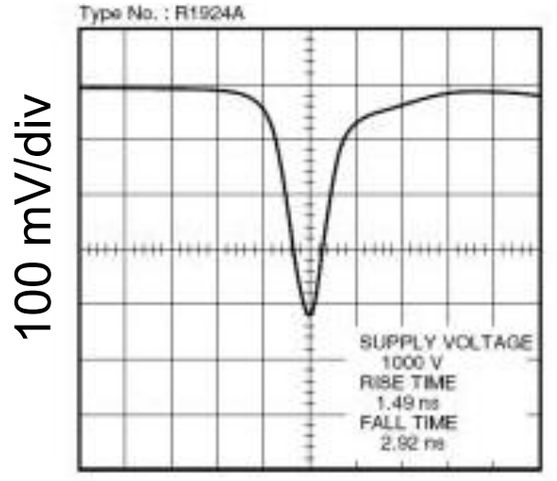

2 ns/div

HAMAMATSU
PHOTON IS OUR BUSINESS

SiPM *versus* PMT

- Solid state *versus* vacuum tube technology
- Comparable gains
- Comparable excess noise
- Comparable photosensitivity in the spectral overlap region
- Greater optimization for PMTs

- Dark count rate per unit active area larger in SiPM
- E & B field immunity in SiPM

HAMAMATSU
PHOTON IS OUR BUSINESS

Operation of an APD

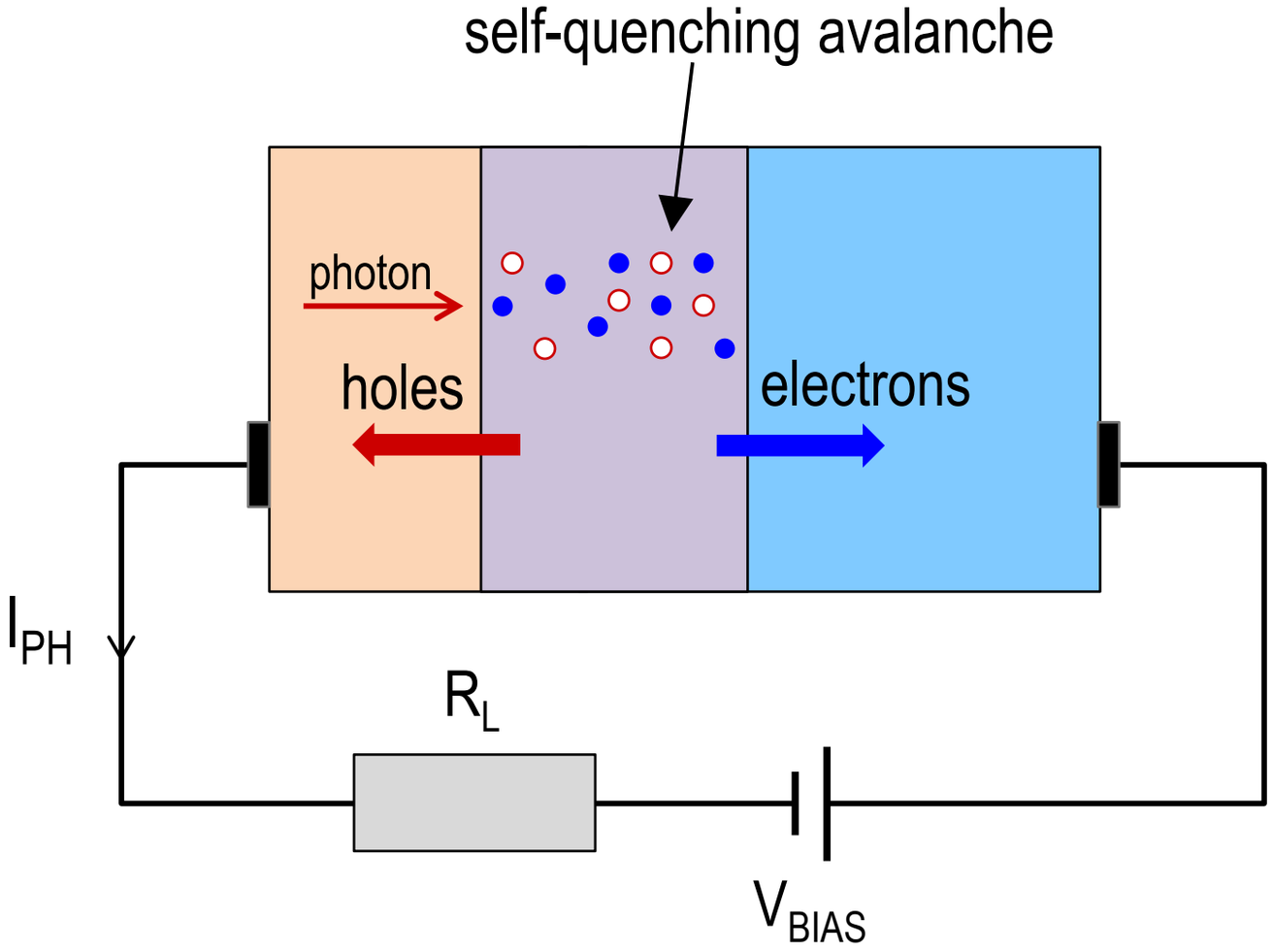

APD biased below breakdown voltage

Single photon can lead up to about 100 of electron-hole pairs

Thus gain up to ~100

Avalanche is self-quenching

SiPM *versus* APD

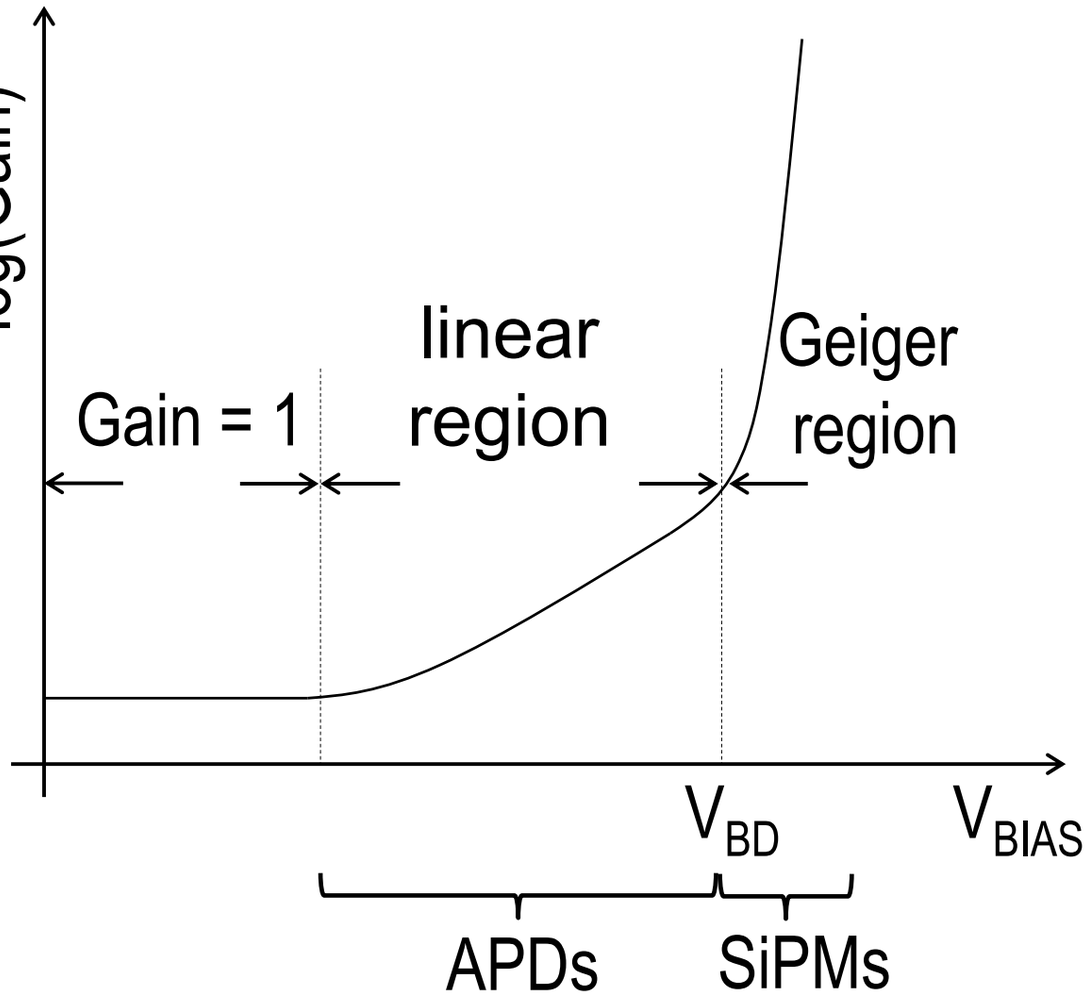

- Differ in construction
- $Gain_{SiPM} >> Gain_{APD}$
- $F_{SiPM} << F_{APD}$

Photosensitivity

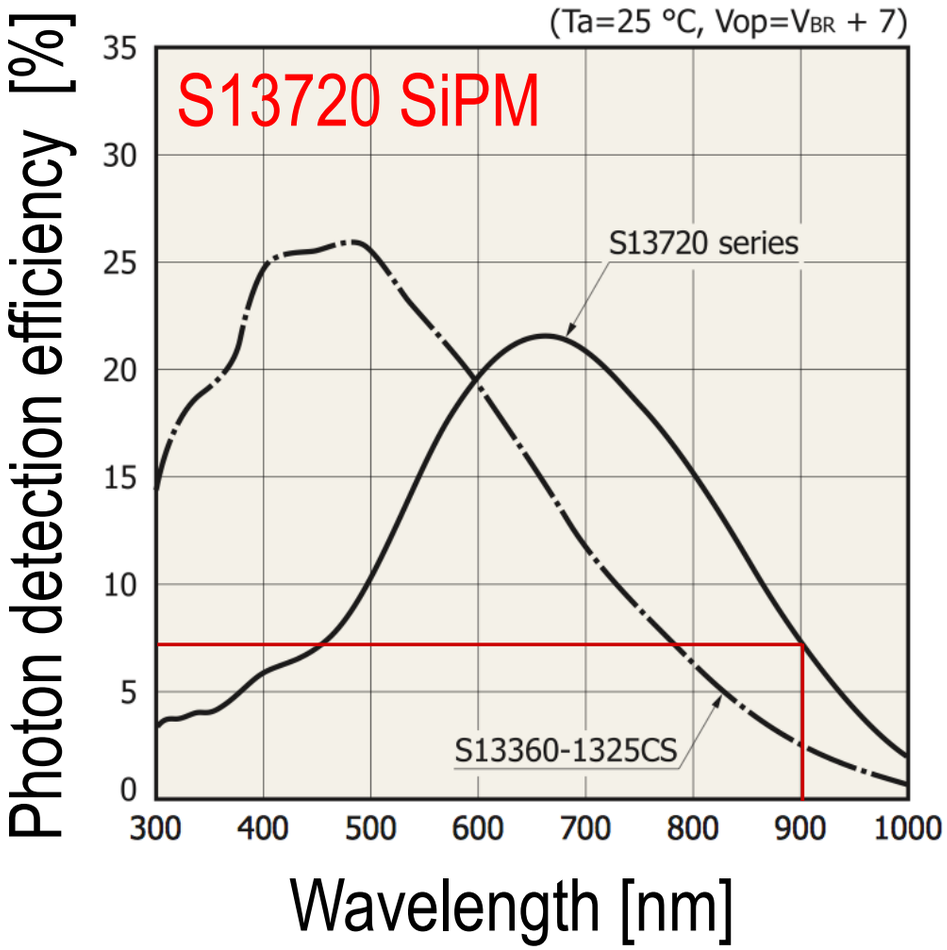

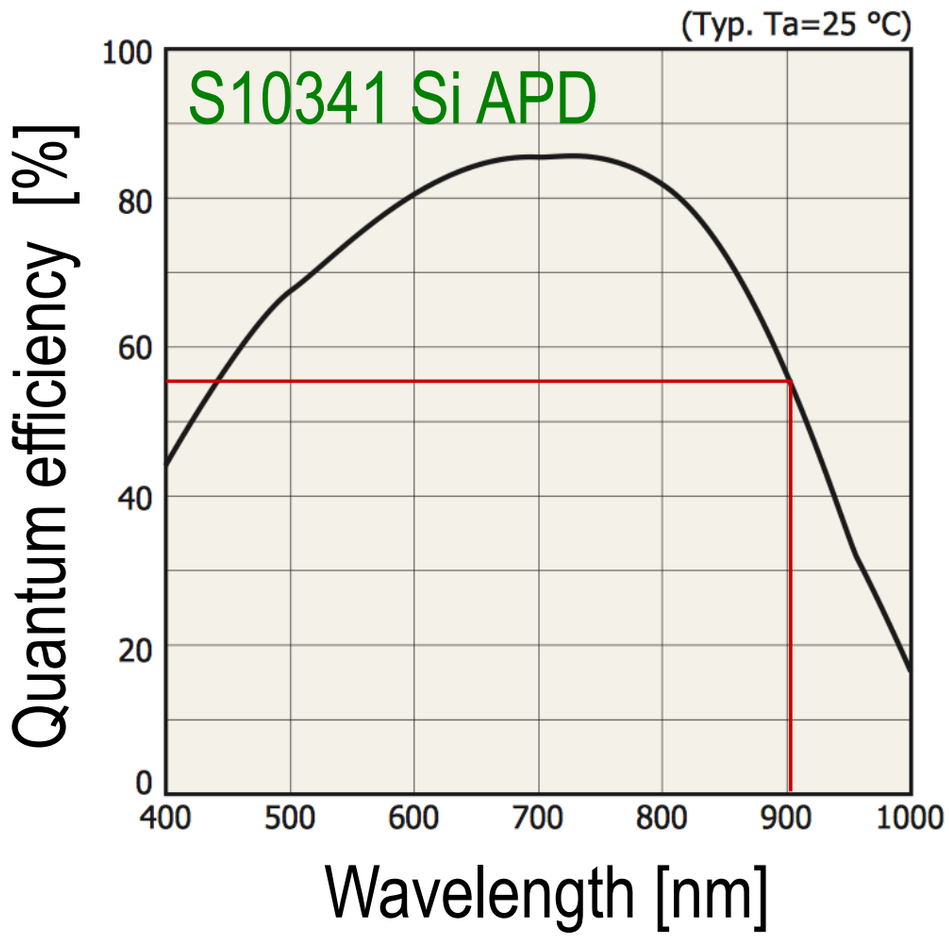

Nuclear Instruments and Methods in Physics Research A 610 (2009) 400–403

Contents lists available at ScienceDirect

Nuclear Instruments and Methods in Physics Research A

journal homepage: www.elsevier.com/locate/nima

First Avalanche-photodiode camera test (FACT): A novel camera using G-APDs for the observation of very high-energy γ-rays with Cherenkov telescopes

I. Braun [a], S.C. Commichau [a,*], M. Rissi [a], M. Backes [b], A. Biland [a], T. Bretz [c], I. Britvitch [a], V. Commichau [a], H. von Gunten [a], D. Hildebrand [a], U. Horisberger [a], D. Kranich [a], E. Lorenz [a,d], W. Lustermann [a], K. Mannheim [c], D. Neise [b], F. Pauss [a], M. Pohl [e], D. Renker [f], W. Rhode [b], U. Röser [a], U. Straumann [g], G. Viertel [a]

Fig. 1. A photomontage of the refurbished HEGRA CT3 telescope with ∼13 m^2 mirror area (La Palma, Canary Islands, Spain).

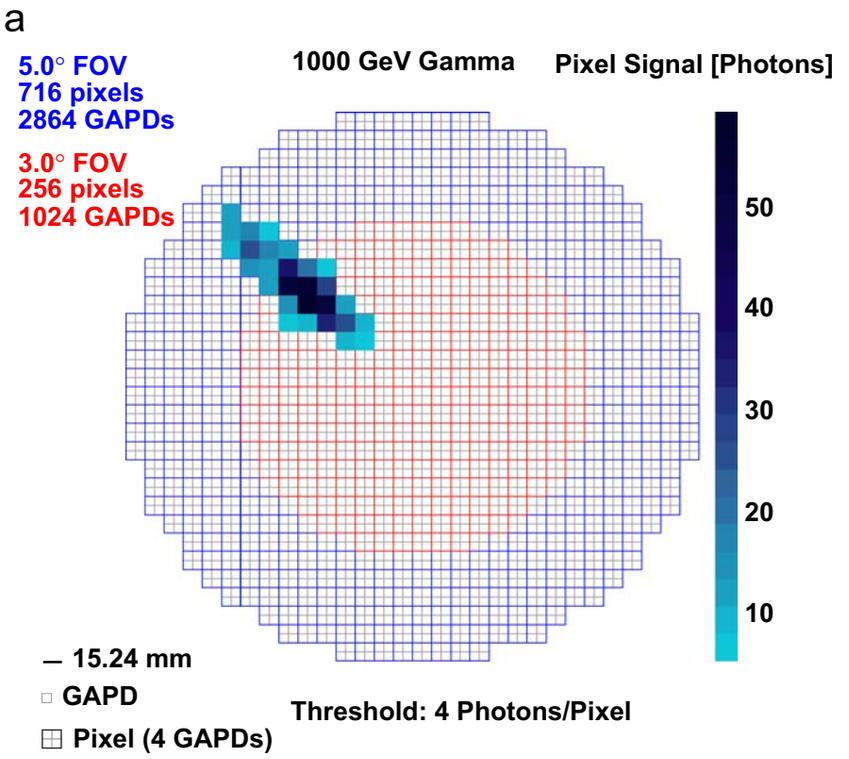

Fig. 3. MC simulated 1000 GeV γ-ray (top) and 1000 GeV proton (bottom) induced showers collected by a 10.5 m^2-mirror. The red (blue) area corresponds to a FoV of 3° (5°), respectively. 2 × 2 G-APDs are grouped to form a pixel. (For interpretation of the references to colour in this figure legend, the reader is referred to the web version of this article.)

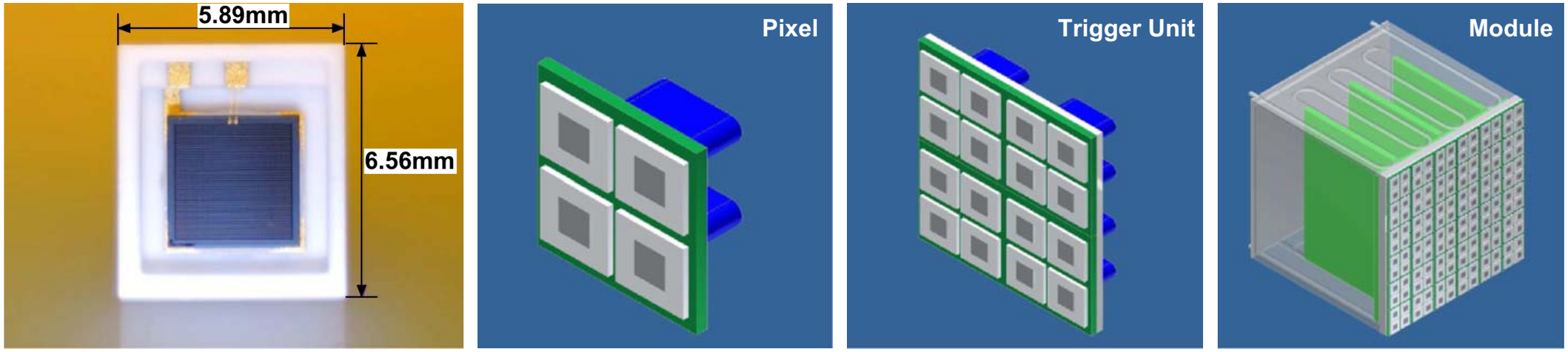

Fig. 5. From left to right: the Hamamatsu G-APD (MPPC S10362-33-100C), layout of a pixel (2 × 2 G-APDs), a trigger unit (16 G-APDs) and a module assembled of 6 × 6 pixels (144 G-APDs).

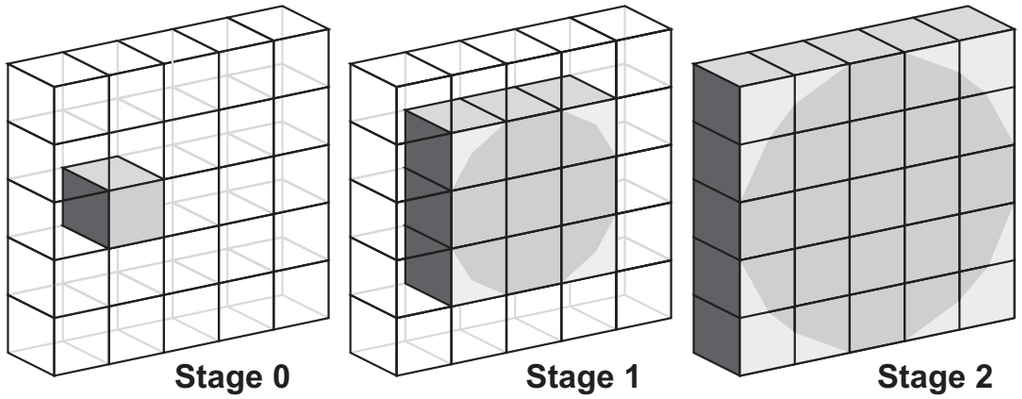

Fig. 6. The camera baseline design.

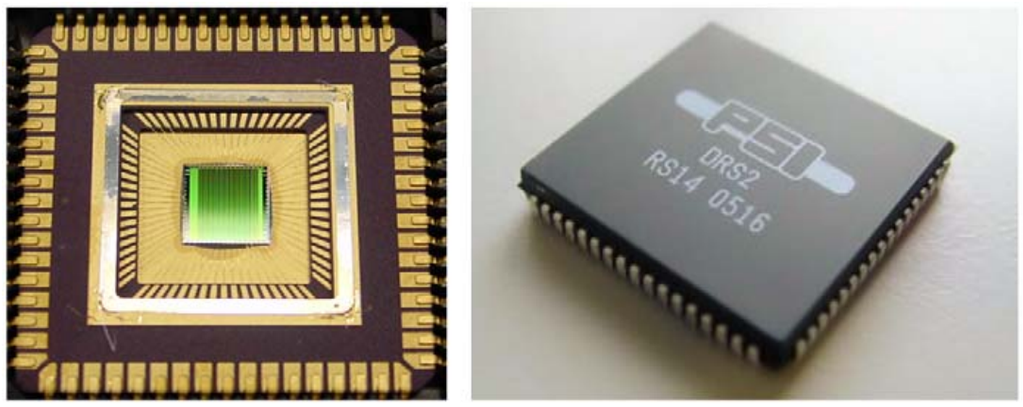

Fig. 7. The DRS chip without and with ceramic package [13].

6. Conclusions

The novel G-APD-based imaging camera is a small but technologically very challenging project. The realization of the project helps to gain expertise on using G-APDs in IACTs. By installing the camera into the refurbished HEGRA CT3 or an equivalent mount, we will be able to perform the first long-term test of a G-APD camera under realistic conditions. The G-APD camera will have an unprecedent sensitivity and it may therefore be considered as a prototype camera for the next generation IACTs, such as CTA [16].

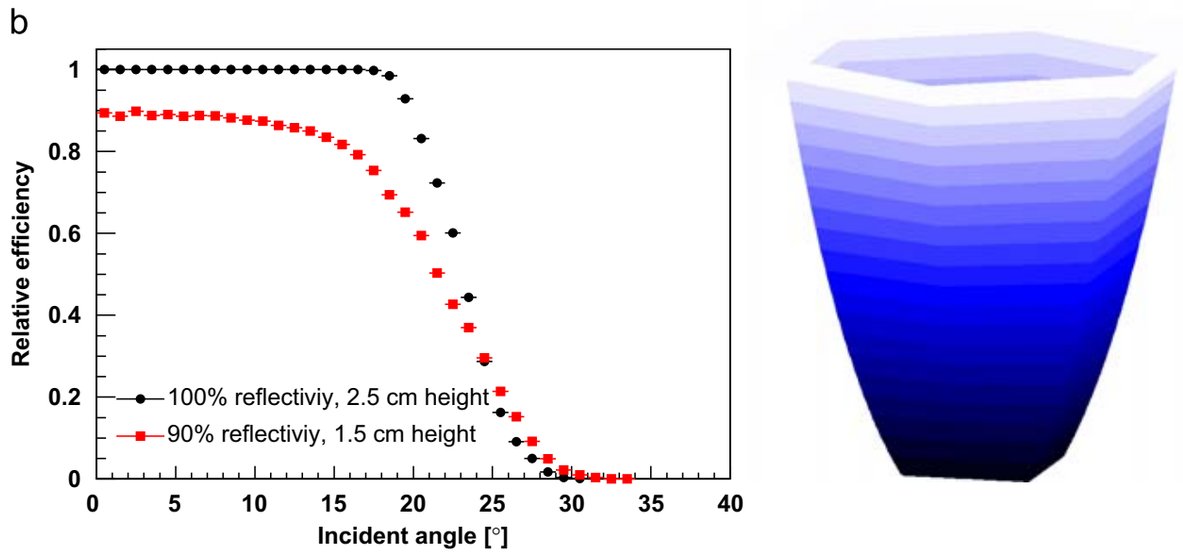

Fig. 4. The light-guide (top) and its efficiency for different reflectivities of the coating and heights (bottom).

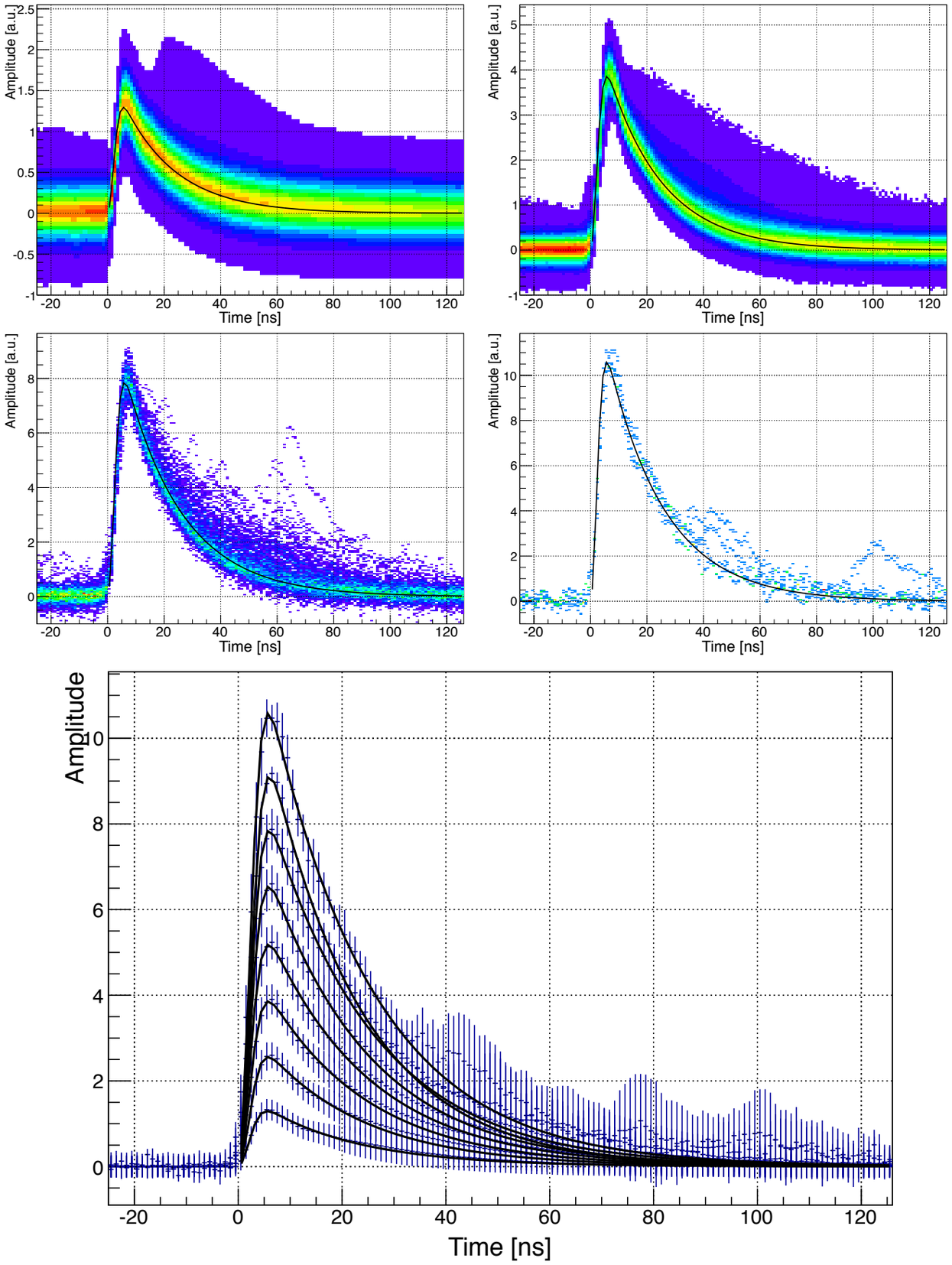

Figure 9. Two dimensional histograms (top) of the sampled waveform. The color scale starts at 0.5% of the maximum bin. The shown multiplicities are 1, 3, 6 and 8 (top left to bottom right). For all multiplicities between one and eight, a profile histogram has been filled (bottom). Fits to the profile histogram are shown as black lines. The inlay shows all eight fits re-normalized with $c_0 = 1$, $c_1 = 0$ and $N = 1$. A good agreement is visible.

Jinst

PUBLISHED BY IOP PUBLISHING FOR SISSA MEDIALAB

RECEIVED: *March 23, 2014*
REVISED: *July 31, 2014*
ACCEPTED: *August 22, 2014*
PUBLISHED: *October 20, 2014*

Calibration and performance of the photon sensor response of FACT — the first G-APD Cherenkov telescope

A. Biland,[a] T. Bretz,[a,1] J. Buß,[b] V. Commichau,[a] L. Djambazov,[a] D. Dorner,[c,1] S. Einecke,[b] D. Eisenacher,[c] J. Freiwald,[b] O. Grimm,[a] H. von Gunten,[a] C. Haller,[a] C. Hempfling,[c] D. Hildebrand,[a] G. Hughes,[a] U. Horisberger,[a] M.L. Knoetig,[a] T. Krähenbühl,[a] W. Lustermann,[a] E. Lyard,[d] K. Mannheim,[c] K. Meier,[c] S. Mueller,[b] D. Neise,[b] A.-K. Overkemping,[b] A. Paravac,[c] F. Pauss,[a] W. Rhode,[b] U. Röser,[a] J.-P. Stucki,[a] T. Steinbring,[c] F. Temme,[b] J. Thaele,[b] P. Vogler,[a] R. Walter[d] and Q. Weitzel[a]

[a] *ETH Zurich, Institute for Particle Physics, Otto-Stern-Weg 5, 8093 Zurich, Switzerland*
[b] *TU Dortmund, Experimental Physics 5, Otto-Hahn-Str. 4, 44221 Dortmund, Germany*
[c] *Institute for Theoretical Physics and Astrophysics, Universität Würzburg, Emil-Fischer-Str. 31, 97074 Würzburg, Germany*
[d] *ISDC Data Center for Astrophysics, University of Geneva, Chemin d'Ecogia 16, 1290 Versoix, Switzerland*

E-mail: thomas.bretz@phys.ethz.ch, dorner@astro.uni-wuerzburg.de

2014 JINST 9 P10012

Nuclear Instruments and Methods in Physics Research A 876 (2017) 17–20

Contents lists available at ScienceDirect

Nuclear Instruments and Methods in Physics Research A

journal homepage: www.elsevier.com/locate/nima

FACT – Status and experience from five years of operation of the first G-APD Cherenkov Telescope

D. Neise [a,*], J. Adam [b], M.L. Ahnen [a], D. Baack [b], M. Balbo [c], M. Bergmann [d], A. Biland [a], M. Blank [d], T. Bretz [a,e], K.A. Brügge [b], J. Buss [b], A. Dmytriiev [c], D. Dorner [d,f], S. Einecke [b], C. Hempfling [d], D. Hildebrand [a], G. Hughes [a], L. Linhoff [b], K. Mannheim [d], S. Müller [a], A. Neronov [c], M. Nöthe [b], A. Paravac [d], F. Pauss [a], W. Rhode [b], A. Shukla [a,d], F. Temme [b], J. Thaele [b], R. Walter [c]

Fig. 1. Photo of the First G-APD Cherenkov Telescope during data taking (P.Vogler). The mirror has an area of ≈9.5 m^2, and the camera consists of 1440 G-APD pixels with a total field of view of about 4.5°.

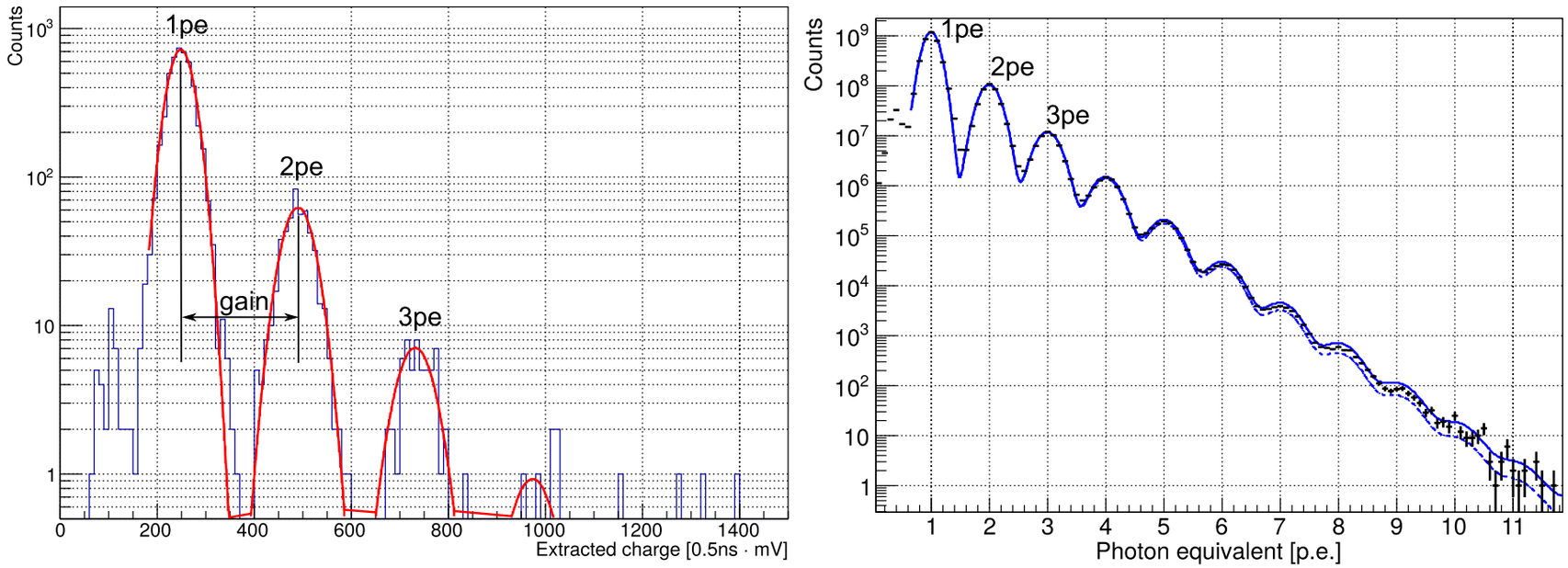

Fig. 2. Dark noise signal spectrum measured with FACT [6]. Photo electron peaks are clearly distinguishable. The distance between the peaks corresponds to the gain for this pixel. The left figure shows the spectrum measured for a single pixel, extracted from 10,000 random triggers. The right plot shows an overlay of spectra of more than 1400 pixels measured over a temperature range of 20 K during more than 6 months.

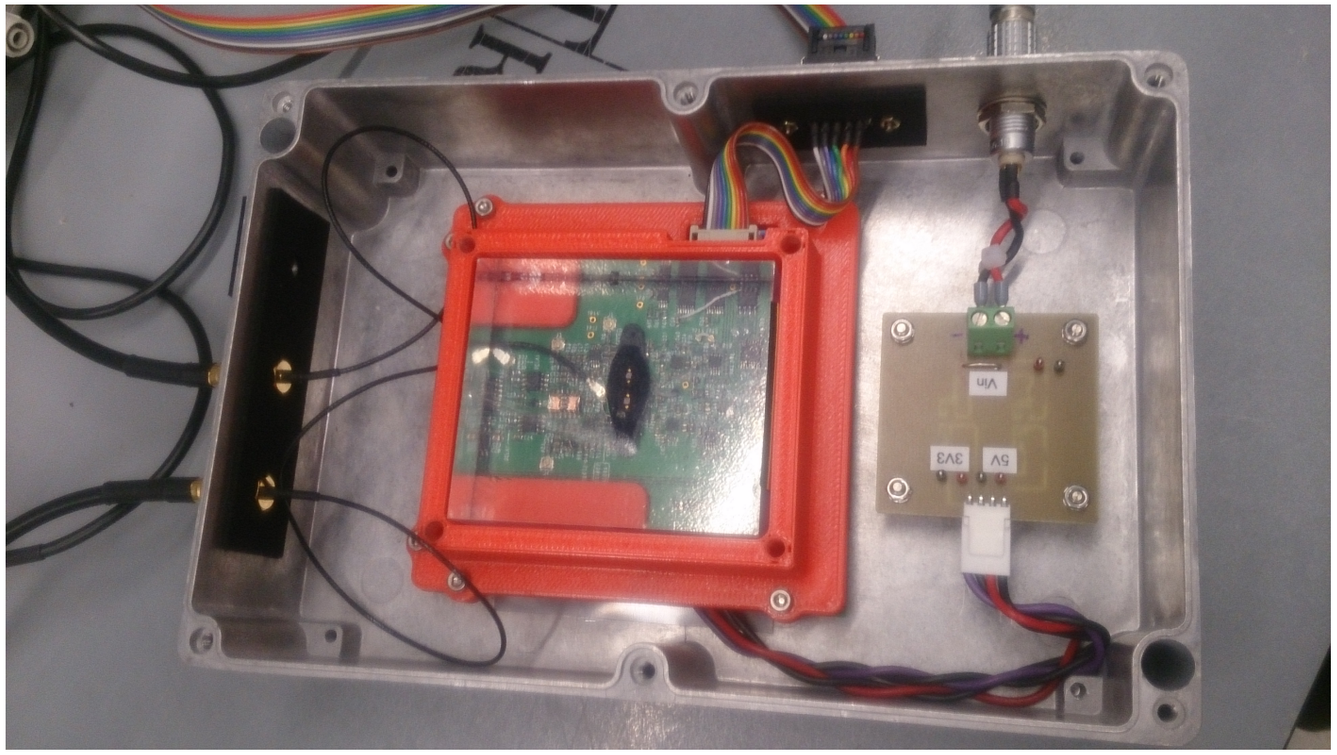

Figure 6.7: Image of the inside of the dark box setup. In the center on top of the board a 3d printed frame is placed to hold the scintillator block in place. On the top and left side of the image exit ports are situated for signal output and command and power input. The module on the right side inside the box is a voltage converter.

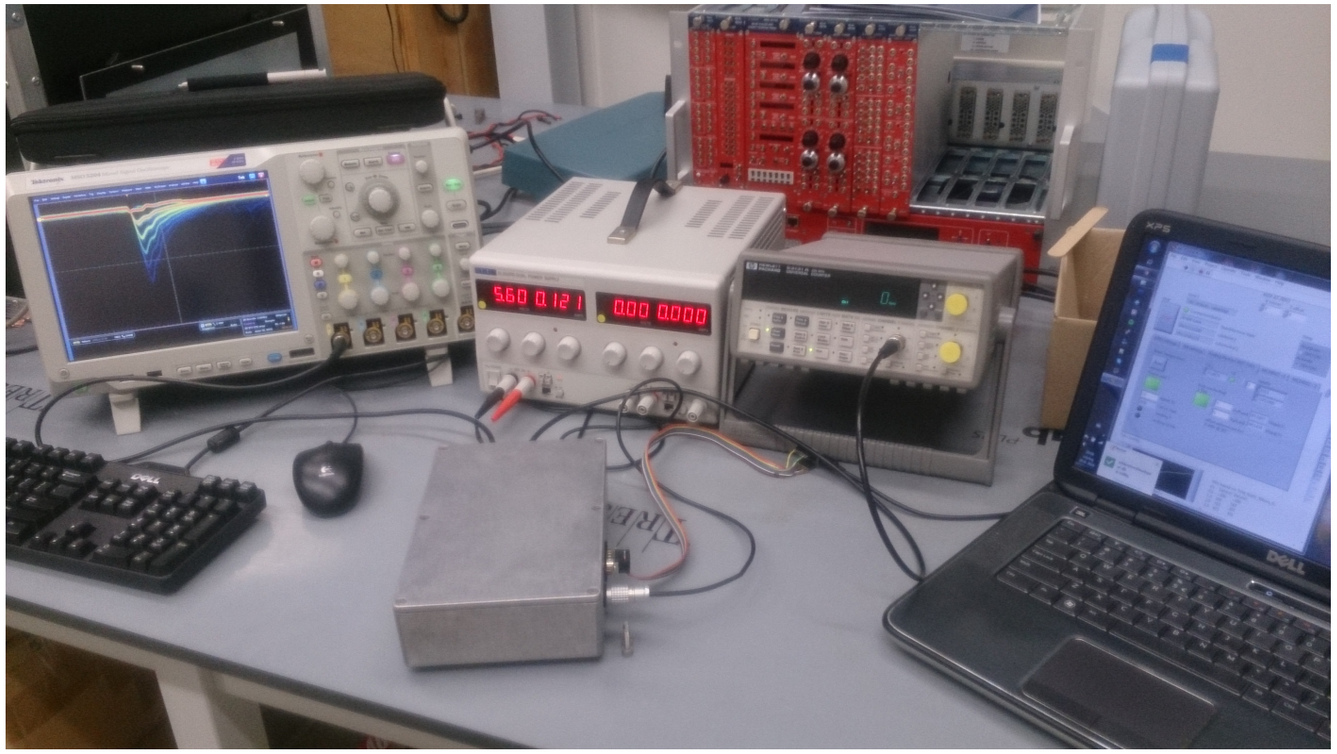

Figure 6.8: Image showing the setup for measuring muons. The dark box in the center is connected to (from left to right) an oscilloscope to check the correct MPPC signal shape, power source to power the board, a counter for measuring coincidence triggers and a laptop with Labview software to control the board (The red module in the back is not used).

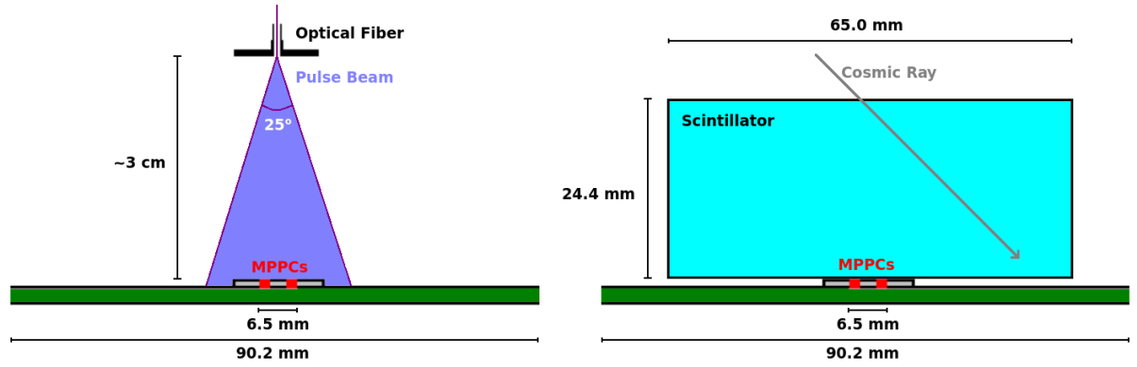

Figure 6.1: Schematic of the two setups described in this chapter. On the left a pulsating light source shines light from an optical fiber to the two MPPCs (section 6.1). On the right a scintillator is mounted on top of the MPPCs so cosmic-ray-induced light can be detected (section 6.2 and 6.3). The depth of scintillator is 75 mm.

Faculty of Science
Physics and Astronomy

Academic year 2015 - 2016
October 20, 2016

Development of a CubeSat Cosmic-Ray Detector

BJARNI PONT

SUPERVISOR: **JÖRG HÖRANDEL**

Radboud University

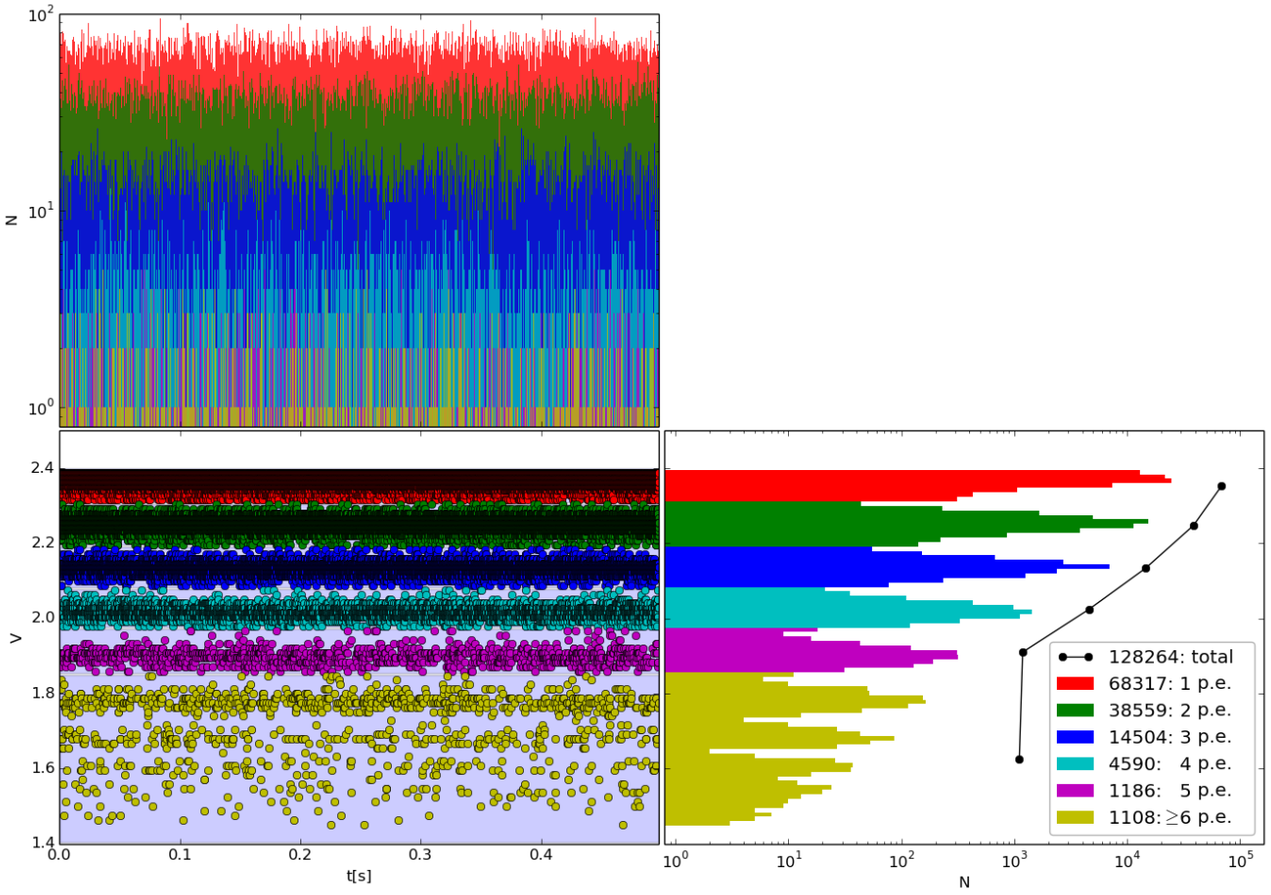

Figure 6.3: Figure similar to figure 5.13. In the lower left graph it shows the detected coincidence events from 1 million pulses from a monochrome pulsating light source with histograms for both axes shown in the top and right graphs. The zero-signal voltage is 2.5 V and the dots in the lower left graph show the identified peaks of a pulse generated by the MPPC. The different colors separate different p.e. levels by their threshold value. The top histogram shows constant flux in time. The right histogram shows the spread of the bands and shows an exponential decrease in number of detections for higher p.e. levels. The black dots show the total count per bin (note that all signals at ≥6 p.e. are stored in the yellow bin). Each pulse is measured in a 500 ns buffer, resulting in a total measurement time of 0.4975 seconds. Coincidence is determined by python code matching MPPC1 and MPPC2 triggers within 10 ns. Note that with larger sample size than in the noise measurement of chapter 5 also the bands above 6 p.e. level now resolve clearly.

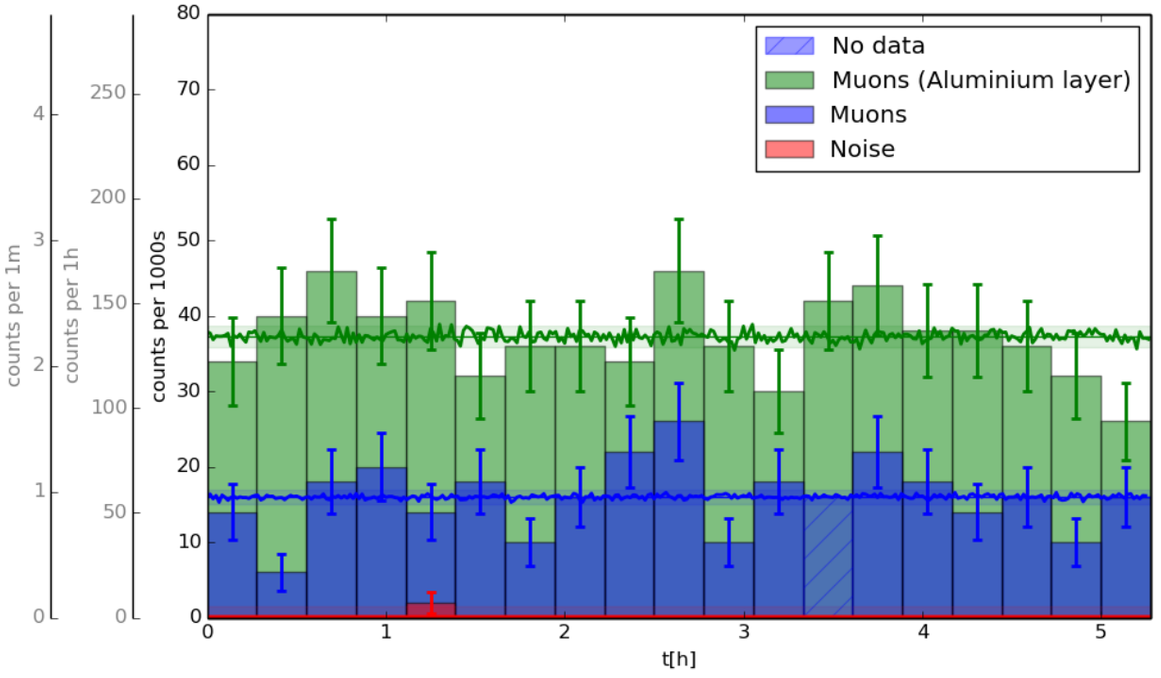

Figure 6.9: Measured muon flux at ≥ 6 p.e. as function of measurement time, binned per 1000 seconds. The blue parts are the measurements done without any reflecting surface around the scintillator. In green the results are shown for a measurement with the block partially covered with aluminium foil, which increased the received light and thus also detected cosmic rays. In red a separate measurement is shown where the scintillator block is removed so the coincidence noise could be measured. The average muon count with 1σ Poisson error is plotted an a thin vertical line with shaded error region. The normalized neutron monitor station data from the Kiel station (Germany) is plotted (spiked line) on top of the average muon count to check that no rapid change in cosmic-ray flux occurred during the measurements [1].

	Muon flux (mHz)	**Noise flux (mHz)**	**Efficiency [%]**	**S/N**
≥ 4 p.e.	78.33 ± 4.44	40.00 ± 4.47	16.08	1.96
≥ 5 p.e.	57.67 ± 3.15	2.00 ± 0.63	11.84	28.84
≥ 6 p.e.	37.26 ± 1.40	0.10 ± 0.07	7.65	372.60
≥ 6 p.e. (no refl.)	16.00 ± 0.94	0.10 ± 0.07	3.29	160.00

Table 6.3: Table showing the measured muon count and noise count per 1000 seconds, the resulting signal to noise ratio, and the muon detection efficiency based on the expected muon flux of 0.487 Hz [12]. Errors are a 1σ Poisson error. Measurements are done for ≥ 4, ≥ 5, and ≥ 6 p.e. with aluminium reflecting layer and for ≥ 6 p.e. without this layer. The last two lines of the table correspond to the data in figure 6.9. Note that the noise is already subtracted from the listed muon count.

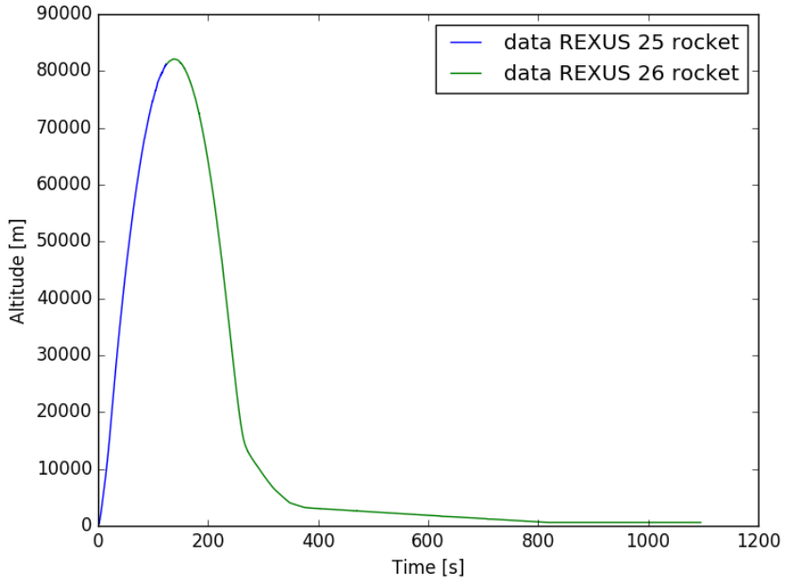

Figure 3.2: Altitude versus time, the time is counted from the liftoff. The altitude up to t=124 seconds was obtained from satellite data from the REXUS 25 flight, the altitude for times larger than 124 seconds into the flight was obtained from the REXUS 26 flight data.

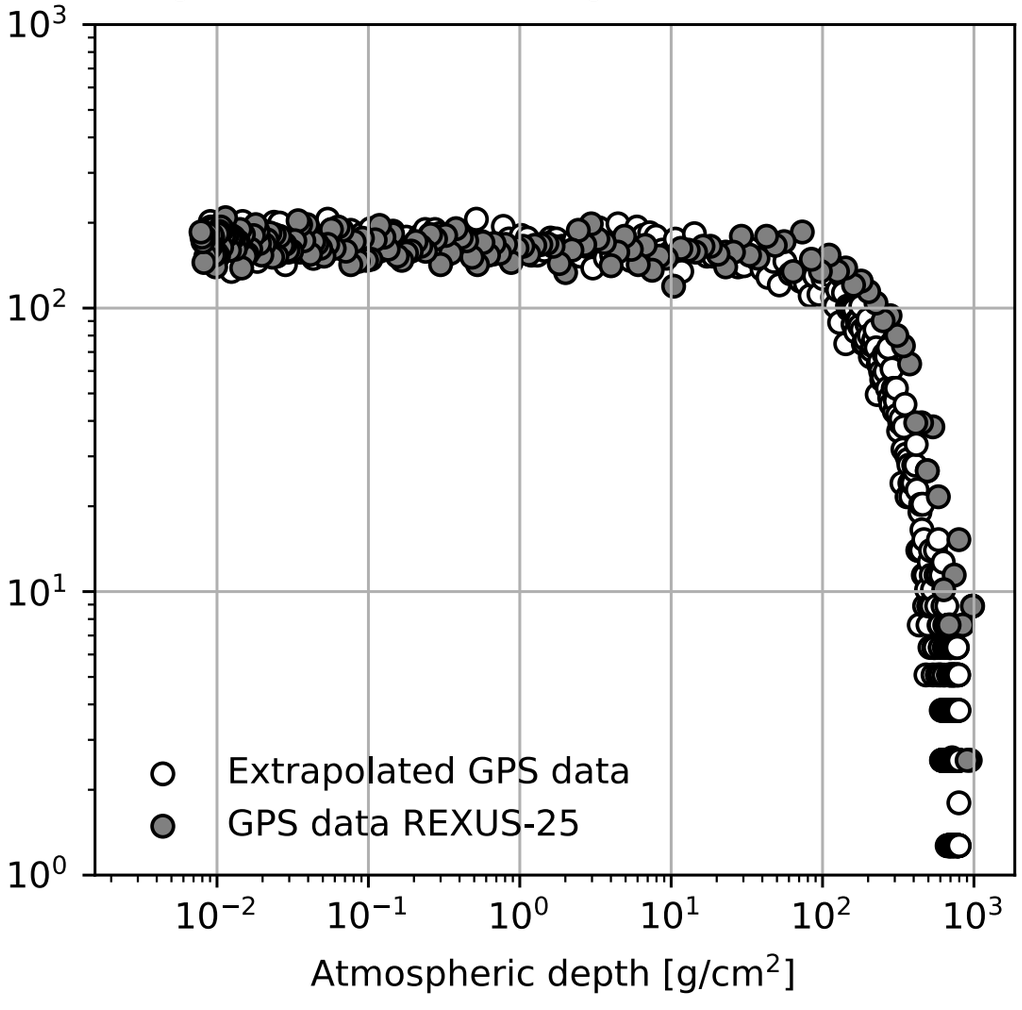

Figure 3.6: Atmospheric depth versus cosmic-ray count rate graphs, the atmospheric depth was obtained from data from the GDAS. Notice that both axes are scaled logarithmically. The points on the right represent near earth point, and the ones on the left are at high altitudes. There is no clear Pfotzer maximum visible in this graph.

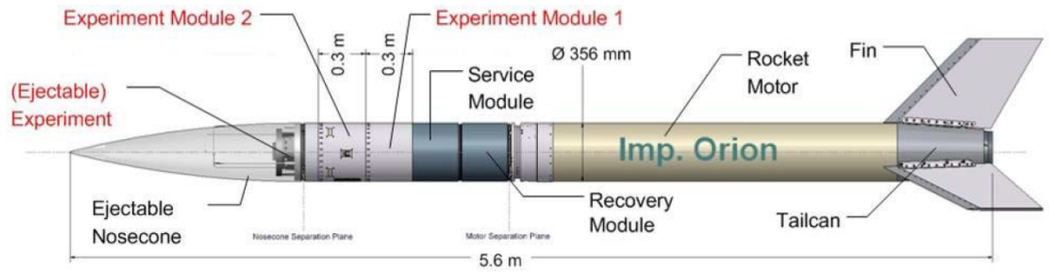

Figure 2.1: A typical configuration of a REXUS sounding rocket [4].

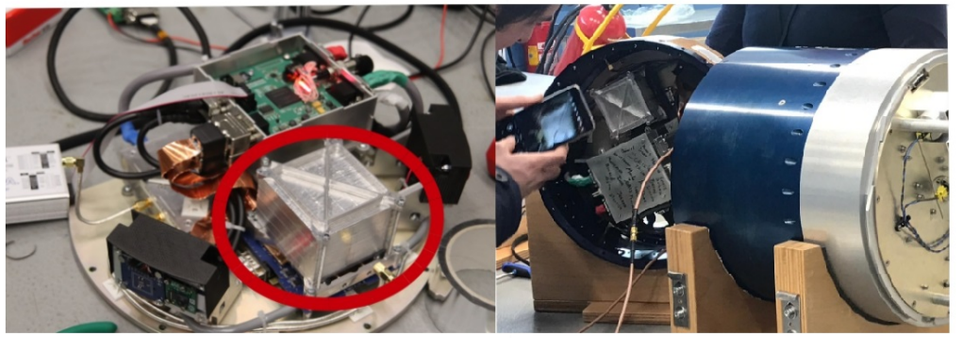

Figure 2.3: The PR3 module, without the outer rim. The circled gray box is the CubeSat cosmic-ray detector. And the PR3 module in the rocket.

Faculty of Science
Physics and Astronomy

Academic year 2019 - 2020
March 1, 2020

Cosmic-ray detection on board of a REXUS rocket

JOCHEM BEURSKENS

SUPERVISORS: **JÖRG R. HÖRANDEL, BJARNI PONT**

Radboud University